NASA TECHNICAL NOTE

NASA TN D-2013

NASA TN D-2013

FULL-SCALE WIND-TUNNEL TEST OF THE VZ-2 VTOL AIRPLANE WITH PARTICULAR REFERENCE TO THE WING STALL PHENOMENA

by Robert G. Mitchell

Langley Research Center
Langley Station, Hampton, Va.

NATIONAL AERONAUTICS AND SPACE ADMINISTRATION • WASHINGTON, D. C. • DECEMBER 1963

TECHNICAL NOTE D-2013

FULL-SCALE WIND-TUNNEL TEST OF THE VZ-2 VTOL AIRPLANE WITH PARTICULAR REFERENCE TO THE WING STALL PHENOMENA

By Robert G. Mitchell

Langley Research Center
Langley Station, Hampton, Va.

NATIONAL AERONAUTICS AND SPACE ADMINISTRATION

NATIONAL AERONAUTICS AND SPACE ADMINISTRATION

TECHNICAL NOTE D-2013

FULL-SCALE WIND-TUNNEL TEST OF THE VZ-2 VTOL AIRPLANE WITH PARTICULAR REFERENCE TO THE WING STALL PHENOMENA

By Robert G. Mitchell

SUMMARY

Flight tests of the VZ-2 tilt-wing VTOL airplane revealed certain unsatisfactory lateral flying characteristics resulting from wing stalling. The present investigation was made to study the aerodynamic and airflow characteristics of the VZ-2 in terms of the stall, and to see whether correlating factors between the wind-tunnel data and flight flying qualities could be found.

A correlation was made at the trim level-flight condition which showed good agreement between the wind-tunnel force data and corresponding flight data on lift and drag. The force-test results, however, showed no apparent correlating factor with the flying-qualities problems associated with wing stall in the transition encountered in the flight tests. For example, there were no pronounced breaks in the lift curves normally associated with wing stall. The tuft-test results did correlate with the acceptable or unsatisfactory flying characteristics for certain flight conditions. There were flight conditions, however, for which the flying characteristics associated with extensive stalling could not be explained by the tuft data.

INTRODUCTION

Flight tests of the VZ-2 tilt-wing VTOL airplane (ref. 1) revealed certain unsatisfactory lateral flying characteristics resulting from wing stalling in the transition. These unsatisfactory characteristics resulted in limitations on the range of possible operating conditions in the transition range, specifically on the permissible rate of descent at various speeds. In certain stalled regions the behavior of the airplane was characterized by wing drop, heavy buffeting, and large yawing motions. (See ref. 2.) Flying the airplane in these conditions was considered unpleasant and, in some cases, hazardous.

The present investigation was made to study the aerodynamic and airflow characteristics of the VZ-2 with particular reference to the stall, and to see whether correlating factors between the wind-tunnel data and flight flying

qualities could be found. The wind-tunnel tests were made in the Langley full-scale wind tunnel. Force tests and tuft tests were made through a range of angles of attack from -12° to 34° and wing incidence angles varying from 25° to 50° to include the range of operating conditions where trouble was encountered in the flight tests. In addition, vibratory stresses in the wing and tail were also measured.

The results are presented for three different wing configurations. The first two configurations tested, the same as those used in flight, were the basic wing and the wing with a modified leading edge. The third configuration tested was the wing with full-span slats to show the effect of slats on the basic aerodynamic characteristics.

SYMBOLS

C_L	lift coefficient, $\frac{\text{Lift}}{qS}$
$C_{L,c}$	corrected lift coefficient, $\frac{\text{Corrected lift}}{q_c S}$
C_D	drag coefficient, $\frac{\text{Scale drag}}{qS}$
$C_{D,c}$	corrected drag coefficient, $\frac{\text{Corrected drag}}{q_c S}$
C_m	pitching-moment coefficient, $\frac{\text{Pitching moment}}{qS\bar{c}}$
q	free-stream dynamic pressure, lb/sq ft
q_c	corrected free-stream dynamic pressure, lb/sq ft
r	rate of climb, ft/min
S	wing area, sq ft
$\bar{c}$	wing chord, ft
α	fuselage angle of attack, deg
α_c	corrected fuselage angle of attack, deg
i_w	wing incidence (measured from line parallel to upper longeron)

R propeller blade radius, ft

V velocity, knots

MODEL

The model used in the investigation was the VZ-2 (Vertol 76) airplane. A drawing of the airplane is shown in figure 1(a) and its principal dimensions and geometric characteristics are given in table I. A photograph of the airplane mounted in the Langley full-scale tunnel is given as figure 2.

The VZ-2, a tilt-wing VTOL airplane, has two three-blade 9.5-foot-diameter propellers with flapping hinges and is powered by a Lycoming T-53 gas-turbine engine rated at 850 horsepower, which drives the propellers through a gear and shaft arrangement.

The wing was pivoted at 0.376 chord and could be rotated to provide a range of incidence angles from 9° to 85°. The basic wing configuration had an NACA 4415 airfoil section. Other wing configurations were the wing with full-span slats and the wing with a modified leading edge. This latter modification consisted of additional thickness near the leading edge which gave an increased leading-edge radius and approximately 6° of leading-edge droop. Drawings of the wing and airfoil sections showing the location of the full-span slats and the modified leading edge are shown in figures 1(b) to 1(d).

The aircraft controls, although not used during the present tests, consisted of an all-movable horizontal tail and conventional ailerons and rudder. Fans are located in the horizontal and vertical tails to provide pitch and yaw control in hovering and low-speed flight; roll control for hovering and low-speed flight was provided by differential variation of the pitch of the two propellers.

Strain gages for the vibratory loads measurements were located at the wing root approximately 10 inches behind the leading edge at the center cutout section and at the root of the vertical-tail spar.

The pitching-moment data are referred to an assumed moment center indicated on figure 1(a). This pitching-moment reference point is located 1.6 inches ahead of and 15.0 inches below the wing pivot.

METHODS AND TESTS

In all tests the collective pitch of the propellers was set so that the thrust equaled the drag for trim level flight, usually at $\alpha_c \approx 0^\circ$ or 2° and the collective pitch was held constant through the angle-of-attack range for any one particular wing incidence. The propeller thrust for trim level flight was different for each wing incidence and was varied by changing the collective pitch. The propeller blade angle β (measured at 0.75R) ranged from 10.3° to 16.6° for the tests.

TABLE I.- GEOMETRIC CHARACTERISTICS OF THE VZ-2 AIRCRAFT

Rotors:	
Diameter, ft	9.5
Blade chord, in.	13
Blade twist (linear, root to tip), deg	19.2
Airfoil section	NACA 0009 with 0.5-inch cusp
Blade taper ratio	1
Solidity, $\frac{nc}{\pi R} = \frac{(\text{No blades})(\text{Blade chord, in.})}{\pi\ (\text{Blade radius, in.})}$	0.218
Distance between propeller axes, ft	14.67
Operational speed, rpm	1,416
Differential pitch, deg	±2
Wing:	
Span (excluding tips), ft	24.88
Chord, ft	4.75
Airfoil section	NACA 4415
Taper ratio	1
Sweep, deg	0
Dihedral, deg	0
Pivot, percent chord	37.6
Ailerons:	
Chord, ft	1.25
Span, ft	5
Tilt range (referenced to upper longeron), deg	9 to 85
Vertical tail:	
Height, ft	5.43
Approximate mean geometric chord, ft	5.90
Sweep at leading edge, deg	28
Basic airfoil section	NACA 0012
Rudder:	
Chord, in.	21.5
Span, in.	58.0
Horizontal tail:	
Span (less tips), ft	9.90
Chord, ft	3.00
Sweep, deg	0
Taper ratio	1
Airfoil section	NACA 0012
Dihedral, deg	0
Length (distance from wing pivot to leading edge of tail), ft	10.475
Hinge point (distance from leading edge), in.	8.3
Control fans:	
Diameter (each fan), ft	2.00
Moment arm about wing pivot (each fan), ft	12.35
Number of blades (each fan)	4
Rotor speed, rpm	5,850
Fuselage length, ft	26.4
Engine	Lycoming T-53

Force tests, flow visualization studies, and vibratory stress measurements were made through a range of angles of attack from -12° to 34° and wing incidence angles varying from 25° to 50° to include the range of operating conditions where the descent limitations were encountered in the flight tests. Tests were conducted for the three different wing design configurations: the basic wing, the wing with a modified leading edge, and the wing with full-span slats. Force tests were made by recording the longitudinal aerodynamic forces and moments on the wind-tunnel scale balance system and motion-picture studies of the stall pattern were made by utilizing wool tufts attached to the upper surface of the wing for flow visualization. Strain-gage records provided a means for analyzing the vibratory component of the normal wing bending moment and the vertical-tail bending moment for an investigation of the vibratory loads. These two moments were analyzed since the flight loads survey indicated that the primary sources of airframe vibratory loads are wing and tail buffeting. (See ref. 3.)

Angle of attack was varied with the hydraulic tail strut, shown in figure 2, which was attached to a plate installed at the aft end of the fuselage. Movement of the strut caused rotation of the aircraft about the landing-gear supports to obtain the desired angle of attack.

The all-movable horizontal tail, conventional ailerons, and rudder were set at 0° and were not deflected during the wind-tunnel tests. The propellers in the horizontal and vertical tails which provide pitch and yaw control in flight were set for essentially zero thrust.

Actuators were installed on the aircraft to allow remote operation of the wing-tilt, collective propeller pitch, and engine mechanisms. During the tests the speed of the engine was constant.

CORRECTIONS

The data have been corrected for tunnel airstream misalinement and for jet-boundary effects, including the influence of the groundboard and blockage. The jet-boundary corrections were made by using a new theory presented in references 4 and 5 for correcting wind-tunnel data of VTOL aircraft. This theory is different from classical wind-tunnel corrections in that it takes into consideration the effect of the large wake deflection experienced by the VTOL-type aircraft. Essentially, this theory divides the lifting system into separate lifting elements and determines the contribution of each element to the overall correction. A more detailed explanation and a sample calculation are given in the appendix.

PRESENTATION OF RESULTS

The figures presenting the results of the present investigation are grouped as follows:

DISCUSSION OF RESULTS

Force Tests

The uncorrected and corrected wind-tunnel force data for the three wing configurations and six wing incidences tested are given in figures 3 to 8. The data are plotted for 25°, 35°, and 45° wing incidence for each of the three configurations in figures 3 to 5, and for 30°, 40°, and 50° wing incidence in figures 6 to 8. This grouping of the data is used to obtain a good separation of the individual curves.

The correlation between the corrected wind-tunnel force data and corresponding flight data is shown in figure 9 for both the basic wing configuration and the wing configuration with a modified leading edge. The correlation was made at the trim level-flight condition. The flight lift coefficients used for the correlation were determined from the weight of the airplane and the flight-path velocity obtained from the flight data. The agreement between the corrected wind-tunnel data and corresponding flight data is good in view of the difficulty often encountered in determining lift coefficients from flight data.

The wing leading-edge droop and the full-span slats had very little effect on the lift and drag curves obtained with the basic wing. (See fig. 10(a).) This was to be expected in one respect since a modification to the wing leading edge does not usually change the location of the basic curves significantly. It was expected, however, that there would be a delay in the onset of stall and an increase in the stall angle of attack as a result of the two modifications. The lift curves of figures 3 to 8, however, do not show any normal or well-defined stall, nor any effect of the leading-edge stall control device on stalling. In fact, inspection of these data shows a different type of lift-drag curves from what might be expected on the basis of previous wind-tunnel tests. The characteristics of a more typical lift-drag polar for a wing-propeller combination are illustrated in figure 10(b). The point where the lift-drag polar begins to diverge from the ideal indicates the onset of stall. As angle of attack is

increased above this point, a point (point X in fig. 10(b)) is reached beyond which the stall progression becomes so rapid that the lift begins to drop off.

It is obvious from figures 3 to 8 that no such breaks as those at point X of figure 10(b) occur in the lift curves. Apparently, the lift component of the propellers caused by an increased angle of attack is greater than the loss of lift resulting from wing stall so that there is no dropoff in total lift. A very gradual stall progression and lack of decided breaks in the lift and drag curves probably resulted to a considerable extent from the fact that, because of the wing-center-section cutout and open fuselage, the wing consisted essentially of two low-aspect-ratio wings and had the characteristic gradual stall progression of low-aspect-ratio wings.

Tuft Tests

The tuft diagrams for the three configurations and six angles of incidence tested are given in figures 11 to 22. The disturbed flow indicated on the figures is defined as flow in which the tufts showed a pendulum-like motion, but not the flow characteristics of the stall. The arrows shown on the diagrams represent the direction of flow on the undisturbed portions of the wing.

In these figures, stall generally occurs over the inboard sections of the wing, and is essentially absent over the outboard sections. This characteristic is caused by propeller slipstream rotation which causes a downwash over the outboard sections of the wing and an upwash over the inboard sections, and also, perhaps because of the wing tip vortex which also tends to keep the tips unstalled.

Figures 11 to 16 give the tuft diagrams for the basic wing and the wing with a modified leading edge, the two configurations that had been flight tested. The diagrams are arranged so that data for the same, or nearly the same, angle of attack are shown side by side for easy comparison. In some cases there was no airflow data for near angles of attack, and in those cases, the sketch of the wing planform has been omitted. Figures 17 to 22 give the tuft diagrams for the full-span-slats configuration.

The general effect of the wing leading-edge modification was to delay the stall and reduce the extent of separation. In general, a further reduction in stall and better symmetrical stall characteristics were obtained with the full-span slats. Reference is made to figure 11 which gives the tuft diagrams for the basic wing and modified leading-edge wing configuration at the 25° incidence. In this figure, the reduction and delay in stall can be seen by observing, in particular, that the inboard sections for the droop-on configuration are essentially unstalled at $\alpha_c \approx 1.7°$ whereas the inboard sections for the basic wing configuration are already heavily stalled at $\alpha_c \approx 0.7°$. The effect of the droop is still evident at $\alpha_c \approx 3.8°$ where the right inboard section is still not as heavily stalled as that for the basic wing configuration.

Another similar example of the delay in stall due to modifying the wing leading edge can be seen in figure 12, which gives the tuft diagrams for the 30° wing incidence. In this figure, the tuft diagrams for both the basic wing configuration and the droop-on configuration show the inboard sections to be

essentially unstalled at $\alpha_c \approx -8.4^\circ$. At angles of attack between -8.4° and 0°, the tuft diagrams show that there was essentially no change in the stalled areas for the droop-on configuration while the stalling of the basic wing had built up progressively to give extensive inboard stalling. The effect of the droop is still evident at $\alpha_c \approx 1.9^\circ$ and $\alpha_c \approx 4^\circ$, the right inboard section still being not as heavily stalled as that for the basic wing configuration.

The characteristic delay in stall over both inboard sections at the 40°, 45°, and 50° wing incidences (figs. 14, 15, and 16) cannot be seen as clearly because of the fact that the left inboard section was heavily stalled over the entire angle-of-attack range covered in the tests. The characteristic delay in the stall over the right inboard section is still evident at the higher wing incidences, however, even after the left inboard section has already stalled. Another improvement in the flow as a result of modifying the wing leading edge was that it cleared up the areas of intermittent stall over the left inboard sections at $\alpha_c \approx 16.2^\circ$ and $\alpha_c \approx 18.5^\circ$ for the 40° wing incidence, and over the inboard sections at $\alpha_c \approx 13^\circ$ and $\alpha_c \approx 15.4^\circ$ for the 50° wing incidence.

The improvements in the stall resulting from the use of the full-span slats on the basic wing can best be seen at the 35° wing incidence. Comparing the tuft diagrams at this wing incidence (fig. 19) with those for the basic wing (fig. 13) the reduction in stall and improvement in the symmetry of the stall is very evident. The characteristic delay in the stall as a result of modifying the wing leading edge can be seen at $\alpha_c \approx 0.4^\circ$ and $\alpha_c \approx 2.6^\circ$. Although the droop had no effect on the inboard stall characteristics above $\alpha_c \approx 4.8^\circ$, the slats did reduce the extent of separation.

Vibratory Stress Tests

The vibratory component of the normal wing bending moment and the vertical-tail bending moment from the vibratory stress tests are not presented, since they seemed to be completely unrelated to the results of the flight tests. It seems likely that the system of mounting the model in the wind tunnel must have completely altered the response of the airplane to the aerodynamic inputs from the turbulent stalled flow, particularly the restraint on the rear part of the fuselage afforded by the rear support strut.

CORRELATION OF WIND-TUNNEL RESULTS WITH FLYING QUALITIES

Flight-Test Results

For correlation of the wind-tunnel results with the flying-qualities results from the flight tests, three conditions were chosen at the wing incidences of 25°, 30°, and 40°. These three conditions were chosen at the trim level-flight condition and are located by circular symbols on the flying-qualities boundary (fig. 23) for both the basic wing configuration and the modified leading-edge configuration. A brief description of this figure will be given to explain its use for the present

analysis. A more detailed explanation of the flight results defining this boundary can be found in reference 2.

Figure 23 shows the rate of climb or descent limitations, defined by pilot opinion, due to unsatisfactory flying qualities observed in the flight tests of the VZ-2 at the Langley Research Center. The rates of climb at the boundary were read visually from a rate-of-climb indicator located in the cockpit.

The horizontal line at zero rate of climb represents the trim level-flight condition. As the transition is made from high-speed level flight ($r = 0$) to the hovering condition with the basic wing, a region with unacceptable or dangerous flying qualities is encountered. This unacceptable flight region is first encountered at a wing incidence of about 25° where the stall first became objectionable, as is indicated by the region with crosshatching. The region of unacceptable dangerous flight, represented by the hatched area, corresponds to flight in which the behavior of the airplane was characterized by wing dropping, pitching, heavy buffeting, and large yawing motions. In trim level flight, this unacceptable region extends through the transition to a wing incidence of about 35° where the flying qualities again become acceptable. Flight in the region above 35° still represents stalled flight but the rolling and yawing moments were no longer severe enough to be considered unacceptable. The three points at 25°, 30°, and 40° wing incidence were chosen as they represent three different types of behavior through the critical flight region for the basic wing configuration and because they show a marked improvement in the flying qualities for the wing with a modified leading edge.

Correlation of Force-Test Results

Previous work, which gave lift-drag curves like that of figure 10(b), indicated that a handling-qualities boundary associated with wing stall might be expected somewhere between the points represented by the circular symbol (stall onset) and the X symbol (major breakdown in lift). As pointed out previously, however, the lift-drag curves for the VZ-2 did not resemble this generalized curve. In general, the tuft data showed the conditions for stall onset had already occurred even at the lowest angles of attack covered in the test. Also, there were no breaks in the lift curves such as are normally associated with wing stall. Even at the highest angles of attack covered in the tests the lift curves had not begun to drop off. Apparently, as mentioned previously, the lift component of the propellers caused by an increased angle of attack is greater than the loss of lift resulting from wing stall. It was not possible, therefore, to correlate the flying-qualities troubles to stall onset or loss in lift as might have been anticipated.

As a second point to check in the force-test results, it might be expected that a stall progression that was abrupt enough to give an abrupt roll-off would show up as a break in the lift curve with an increase in the drag. The flight results indicate such a roll-off with a wing drop or unsymmetrical stall occurring in level flight for the 25° condition with the basic wing. (See fig. 23.) The inspection of the lift curve for this condition (fig. 3), however, shows that no such break in the lift curve occurs.

Correlation of Tuft-Test Results

The tuft-pattern analysis was made to see whether there were any stall phenomena that would correlate with the flying qualities at the three trim level-flight conditions of particular interest at 25°, 30°, and 40° wing incidence.

Basic wing.- For the 25° incidence with the basic wing, the flight results indicate a wing drop, or unsymmetrical stall, at the trim level-flight condition. (See fig. 23.) The wind-tunnel data of figure 3 show that in these tests the angle of attack for zero drag was 2°. The tuft diagrams at $\alpha_c \approx -0.3^\circ$ and $\alpha_c \approx 0.7^\circ$ indicate a flow phenomena which would be expected to cause a wing drop at about $\alpha_c \approx 0.7^\circ$. They show an abrupt change in the stall occurring over the left inboard section, while flow over the right inboard section remains essentially unchanged. This result is considered to occur close enough to the angle of attack for trim level flight to constitute a reasonable correlation with the flight results.

For the 30° incidence condition with the basic wing (see fig. 12), the tuft diagrams show the inboard panels are heavily stalled at the trim level-flight condition $\alpha_c \approx 2^\circ$ and that the stall is reasonably symmetrical. The difficulties experienced in flight at this condition were those associated with a well-developed-stall wallowing motion in roll and yaw and possibly heavy buffeting. It is difficult to see how these conditions could be recognized from the tuft tests since there were conditions at higher wing incidences in which extensive stalling did not produce unacceptable flying qualities. For example, with the basic wing at 40°, 45°, and 50° incidence in the trim level-flight condition, which occurred at about $\alpha_c \approx 0^\circ$, -1°, and -2°, respectively, the tuft tests showed that the wing was almost completely stalled inboard of the nacelles, but the flying-qualities results of figure 23 do not indicate unsatisfactory characteristics.

For the 40° incidence condition with the basic wing (fig. 14), trim level flight occurs at $\alpha_c \approx 0^\circ$. The tuft diagram at $\alpha_c \approx 0.6^\circ$ shows both sections heavily stalled with no appreciable change in stall occurring from $\alpha_c \approx -4.4^\circ$ to $\alpha_c \approx 0.6^\circ$. Flight results (fig. 23) show acceptable flying qualities at this trim level-flight condition. The difference in the flying qualities between this $i_w = 40^\circ$ condition and the $i_w = 30^\circ$ incidence condition which also had a well-developed stall might be attributed, to a certain extent, to a difference in the buffet intensity at these two trim level-flight conditions or to a difference in the severity of the general wallowing motions of the airplane because of the difference in airspeed. Flight results show the buffet intensity to be about one-half as great at $i_w = 40^\circ$ as at the $i_w = 30^\circ$ basic wing condition. (See fig. 3, ref. 3.)

Wing with modified leading edge.- For the 25° incidence condition with the modified leading-edge wing (see fig. 11), the trim level-flight condition occurs at $\alpha_c \approx 2^\circ$. For angles of attack in this range ($\alpha_c \approx -0.4^\circ$ to 1.7°) the tuft diagrams show no rapidly developing asymmetry in the stall over either the right or left inboard sections. For this reason the airplane would not be expected to experience any wing drop or wallowing motion at the trim level-flight condition.

This result is in agreement with the flight results which show acceptable flying qualities at this wing incidence and trim level-flight condition. (See fig. 23.)

For the 30° incidence condition with modified leading-edge wing (see fig. 12), the trim level-flight condition occurs at $\alpha_c \approx 1.9°$. The tuft diagrams show that between $\alpha_c \approx -0.2°$ and $\alpha_c \approx 1.9°$, the left inboard panel becomes heavily stalled and flow over the right inboard panel remains essentially unchanged. At first glance, this unsymmetrical stall progression seems to be at odds with the acceptable flying qualities observed in flight at this trim level-flight condition. (See fig. 23.) It is possible, however, that the stall over the left inboard section occurred with sufficient graduation over the 2° angle-of-attack range so that it did not result in an abrupt wing dropping or other unacceptable flying qualities.

For the 40° incidence condition with the modified leading-edge wing (fig. 15), the trim level-flight condition occurs at $\alpha_c \approx -1.4°$. The tuft diagram at $\alpha_c \approx -3.7°$ (representing a 200 feet per minute rate of climb) shows intermittent stall occurring over the right inboard section, the left inboard section being heavily stalled. At $\alpha_c \approx 0.7°$ (a 100 feet per minute rate of descent), the tuft data show the right inboard section heavily stalled. It is difficult to say what the stall picture would look like at the trim level-flight condition. For this reason, there does not seem to be any way to explain the observed satisfactory flying qualities with the tuft-test data.

The correlation of the tuft-test results with regard to the trim level-flight flying qualities may be summarized by observing that, although the tuft data did help to substantiate, or explain, the acceptable or unsatisfactory flying qualities for certain of the flight conditions, there were the flight conditions associated with well-developed stalls for which the flying characteristics could not be explained by the tuft data.

CONCLUDING REMARKS

A correlation made at the trim level-flight condition showed a good agreement between the wind-tunnel force data and corresponding flight data on lift and drag. The force-test results, however, showed no apparent correlating factor with the flying-qualities problems associated with wing stall in the transition encountered in the flight tests. For example, there were no pronounced breaks in the lift curves normally associated with wing stall. The tuft-test results did help to substantiate, or explain, the acceptable or unsatisfactory flying characteristics for certain flight conditions. There were flight conditions, however, for which the flying characteristics associated with extensive stalling could not be explained by the tuft data.

Langley Research Center,
National Aeronautics and Space Administration,
Langley Station, Hampton, Va., July 23, 1963.

APPENDIX

METHOD USED FOR CORRECTING DATA

Symbols

The symbols used in the method for correcting the data are as follows:

A_m	momentum area of lifting system, sq ft
A_t	cross-sectional area of wind-tunnel test section, sq ft
b	wing span, ft
C_D	drag coefficient, D/q_tS
$C_{D,c}$	corrected drag coefficient, D_c/q_cS
C_L	lift coefficient, L/q_tS
$C_{L,c}$	corrected lift coefficient, L_c/q_cS
D	drag, lb
D_c	corrected drag, lb
D_i	induced drag, lb (Note that a forward-directed thrust is considered in this context as a negative "induced" drag)
L	lift, lb
L_c	corrected lift, lb
M_t	mass flow through wind tunnel, $\rho A_t V$, slugs/sec
M_u	longitudinal mass flow due to induced drag, $\rho A_m u_o$, slugs/sec
M_w	vertical mass flow due to lift, $\rho A_m w_o$, slugs/sec
n	ratio of final induced velocities in far wake to initial induced velocities at model
q_c	corrected dynamic pressure, lb/sq ft
q_t	free-stream dynamic pressure, lb/sq ft
R	propeller blade radius, ft
S	area of wing, sq ft

T	thrust, lb
u_o	mean or momentum-theory value of longitudinal induced velocity at model, positive rearward, ft/sec
Δu	total longitudinal interference velocity, positive rearward, ft/sec
Δu_D	longitudinal velocity due to induced drag, positive rearward, ft/sec
$\delta_{u,D}$	interference factor for longitudinal interference velocity due to drag
Δu_L	longitudinal interference velocity due to lift, positive rearward, ft/sec
$\delta_{u,L}$	interference factor for longitudinal interference velocity due to lift
V	wind-tunnel velocity, ft/sec
V_c	corrected velocity, ft/sec
w_h	reference velocity, positive upward, $-\sqrt{\frac{L}{n\rho A_m}}$, ft/sec
w_o	mean or momentum-theory value of vertical induced velocity, positive upward, ft/sec
Δw	total vertical interference velocity, positive upward, ft/sec
Δw_D	vertical interference velocity due to induced drag, positive upward, ft/sec
$\delta_{w,D}$	interference factor for vertical interference velocity due to drag
Δw_L	vertical interference velocity due to lift, positive upward, ft/sec
$\delta_{w,L}$	interference factor for vertical interference velocity due to lift
α	angle of attack, deg
α_c	corrected angle of attack, deg
α_w	wing angle, $i_w + \alpha$
$\Delta\alpha$	change in angle of attack due to interference, deg
i_w	wing incidence
ρ	mass density of air, slugs/cu ft

χ wake skew angle; angle between vertical axis (negative direction) and wake center line, positive rearward, deg

β wind-tunnel stream angle correction, deg

p propeller

w wing

Subscripts:

1 first

2 second

eff effective

m model

p propeller

r rake

w wing

p/p propeller on propeller on itself

p/w propeller on wing

p/r propeller on rake

w/w wing on wing on itself

w/p wing on propeller

w/r wing on rake

Introduction

Jet-boundary corrections were made by using a theory outlined in references 4 and 5. This theory divides the lifting system into separate lifting elements. The induced drag-lift ratio D_i/L, the reference velocity w_h, and the wind-tunnel velocity V, are determined for each element at each angle of attack. The interference velocities at each element at a particular angle of attack are then determined. At the particular angle of attack, the interference velocities for each element are added and used to obtain the correction.

For the VZ-2, the lifting system was considered to be four lifting elements: two propeller elements and two wing elements. The two propeller lifting elements

acting at the propeller disk centers were separated by a distance equal approximately to the wind-tunnel semi-height (15 feet). The two wing lifting elements were located 32 inches behind the two propeller elements and were considered to be acting at the wing quarter-chord line.

Below is a planform view of the four lifting elements with their spacing dimensions shown. The propeller lifting elements are designated p_1 and p_2, and the wing lifting elements are designated w_1 and w_2. The wind-tunnel velocity is shown as vector V. A total static tube rake used to read the tunnel velocity is shown with its location from the model.

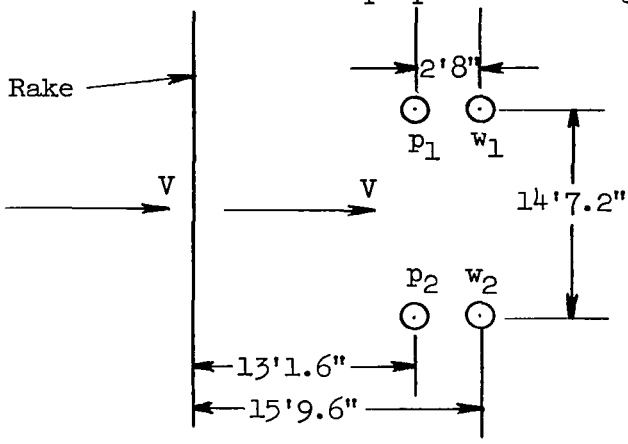

Because of the symmetry of the system only one-half of the lifting system need be considered. The interference effect of propeller elements p_2 on p_1 and p_1 on itself is called the "effect of propeller on propeller on itself." Likewise, the interference effect of wing elements w_2 on w_1 and w_1 on itself is called the "effect of wing on wing on itself." The interference effect of elements w_1 on p_1 is called the "effect of wing on propeller." Likewise, the interference effect of elements p_1 on w_1 is called the "effect of propeller on wing."

The steps of the procedure are described and a sample calculation given.

Steps of Procedure

The steps of the procedure are as follows:

(1) Determine the induced drag-lift ratio D_i/L. According to the author of the described theory, a forward-directed thrust is considered to be a negative "induced" drag. The present application considers the horizontal component of thrust as the induced drag and uses the vertical thrust component as the lift to obtain D_i/L for the propeller. With this terminology, the drag on the wing is considered in this application to be a positive induced drag. This drag together with the wing lift is used to obtain D_i/L for the wing.

(2) Determine the reference velocity w_h from $w_h = -\sqrt{\frac{L}{n\rho A_m}}$.

(3) Determine V/w_h, the ratio of tunnel velocity to reference velocity.

(4) Find w_o/w_h from nomographic chart in reference 4. The chart plots V/w_h against w_o/w_h with D_i/L as a parameter.

(5) Determine the ratio of tunnel velocity to momentum theory vertical induced velocity V/w_o where $V/w_o = \frac{V/w_h}{w_o/w_h}$.

(6) Find χ from chart given in reference 4. The chart plots χ against w_o/w_h.

(7) Find $\delta_{w,L}$ from tables presented in reference 5.

(8) Likewise, find $\delta_{u,L}$, $\delta_{w,D}$, and $\delta_{u,D}$ from tables in reference 5.

(9) Determine M_w/M_t, the ratio of vertical mass flow due to lift to mass flow through the tunnel, where $M_w/M_t = \frac{A_m/A_t}{V/w_o}$.

(10) Determine M_u/M_t, the ratio of horizontal mass flow due to induced drag to mass flow through the tunnel, from $M_u/M_t = \left(M_w/M_t\right)\left(D_i/L\right)$.

(11) Determine $\Delta w_L/V$, the ratio vertical interference velocity due to lift to the tunnel velocity, from $\Delta w_L/V = \delta_{w,L}\left(M_w/M_t\right)$.

(12) Determine $\Delta u_L/V$, the ratio horizontal interference velocity due to lift to the tunnel velocity, from $\Delta u_L/V = \delta_{u,L}\left(M_w/M_t\right)$.

(13) Determine $\Delta w_D/V$, the ratio vertical interference velocity due to drag to the tunnel velocity, from $\Delta w_D/V = \delta_{w,D}\left(M_u/M_t\right)$.

(14) Determine $\Delta u_D/V$, the ratio horizontal interference velocity due to drag to the tunnel velocity, from $\Delta u_D/V = \delta_{u,D}\left(M_u/M_t\right)$.

(15) Determine $\Delta w/V$, the ratio total vertical interference velocity to the tunnel velocity, from $\Delta w/V = \Delta w_L/V + \Delta w_D/V$.

(16) Determine $\Delta u/V$, the ratio total horizontal interference velocity to the tunnel velocity, from $\Delta u/V = \Delta u_L/V + \Delta u_D/V$.

(17) Determine $\Delta\alpha$ from $\Delta\alpha = \tan^{-1}\frac{\Delta w/V}{1 + \Delta u/V}$.

(18) Determine α_c from $\alpha_c = \alpha + \Delta\alpha$.

(19) Determine q_c/q_t, from $q_c/q_t = (1 + \Delta u/V)^2 + (\Delta w/V)^2$. This is the corrected dynamic pressure ratio when the velocity is measured at the model. When the velocity is measured at a rake, corrections for the influence of the model on the rake must be made. The proper correction factor to apply is equal to the difference between the correction factors at the model and the rake. For this case,

$$q_c/q_t = \left[1 + (\Delta u/V)_{eff}\right]^2 + \left[(\Delta w/V)_{eff}\right]^2$$

where

$$(\Delta u/V)_{eff} = (\Delta u/V)_m - (\Delta u/V)_r$$

and

$$(\Delta w/V)_{eff} = (\Delta w/V)_m - (\Delta w/V)_r$$

(20) Determine q_c from $q_c = (q_c/q_t)q_t$.

(21) Determine L_c and D_c, from

$$L_c = L \cos \Delta\alpha - D \sin \Delta\alpha$$

$$D_c = L \sin \Delta\alpha + D \cos \Delta\alpha$$

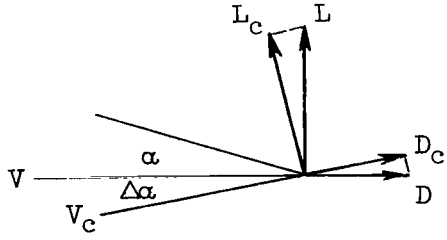

Since lift and drag are always defined as being perpendicular and parallel, respectively, to the relative wind, it is necessary to resolve the lift and drag read to the new effective velocity V_c. (See sketch.)

(22) Determine $C_{L,c}$ and $C_{D,c}$ from

$$C_{L,c} = \frac{L_c}{q_c S}$$

$$C_{D,c} = \frac{D_c}{q_c S}$$

Sample Calculation

A sample calculation was made for the basic wing configuration. The results of the wind-tunnel tests and other variables used in the computation are as follows:

L = 3,357 lb (total lift read on scales)

D = 484 lb (total drag read on scales)

$C_L = 5.09$

$C_D = 0.734$

$T = 1{,}366$ lb (thrust of one propeller; propeller data taken from isolated propeller tests, ref. 6)

$q_t = 5.58$ lb/sq ft

$V = 69.1$ ft/sec

$\alpha = 12^\circ$

$i_w = 40^\circ$

$\alpha_w = 52^\circ$

$S = 118.2$ sq ft

$(A_m)_w = \pi\left(\frac{b}{2}\right)^2 = 470$ sq ft

$(A_m)_p = \pi R^2 = 71$ sq ft, each propeller

$n = 2.0$

$A_t = 1{,}607$ sq ft

$\rho = 0.002338$ slug/cu ft

$\beta = -0.5^\circ$

Effect of propeller on propeller on itself.- The interference velocities at propeller element p_1, due to its own presence in the wind tunnel and the additional interference at p_1 due to the presence of propeller element p_2, were determined. The total propeller interference at p_1 is then the sum of the two interferences and is determined in the calculation for the "effect of propeller on propeller on itself." The mathematics involved in this computation is as follows:

(1) $L_p = T \sin \alpha_w = 1{,}366(0.7880) = 1{,}076.4$ lb

$D_p = T \cos \alpha_w = 1{,}366(0.6157) = 841.0$ lb

$(D_i)_p = -D_p = -841.0$ lb

$(D_i/L)_p = -841.0/1{,}076.4 = -0.78$

(2) $w_h = -\sqrt{\frac{L_p}{n\rho(A_m)_p}} = -\sqrt{\frac{1,076.4}{(2)(0.002338)(71)}} = -56.9$ ft/sec

(3) $V/w_h = 69.1/-56.9 = -1.21$

(4) $w_o/w_h = 0.576$ (from fig. 6, ref. 4)

(5) $V/w_o = \frac{V/w_h}{w_o/w_h} = -1.21/0.576 = -2.10$

(6) $\chi = 70.4^\circ$ (from fig. 7, ref. 4)

(7) $\delta_{w,L} = -0.142$

(8) $\delta_{u,L} = 0.970$

$\delta_{w,D} = -0.900$

$\delta_{u,D} = 0.336$

} From charts prepared by using tables in reference 5.

(9) $M_w/M_t = \frac{(A_m)_p/A_t}{V/w_o} = \frac{71/1,607}{-2.10} = -0.02104$

(10) $M_u/M_t = M_w/M_t(D_i/L)_p = (-0.02104)(-0.78) = 0.01641$

(11) $\Delta w_L/V = \delta_{w,L}(M_w/M_t) = (-0.142)(-0.02104) = 0.00299$

(12) $\Delta u_L/V = \delta_{u,L}(M_w/M_t) = (0.970)(-0.02104) = -0.02041$

(13) $\Delta w_D/V = \delta_{w,D}(M_u/M_t) = (-0.900)(0.01641) = -0.01477$

(14) $\Delta u_D/V = \delta_{u,D}(M_u/M_t) = (0.336)(0.01641) = 0.00551$

(15) $(\Delta w/V)_{p/p} = -0.01178$

(16) $(\Delta u/V)_{p/p} = -0.01490$

} To be used for composite correction.

Effect of wing on propeller.- Because of the presence of the wing element w_1, there is an additional interference velocity at the propeller element p_1. This interference is determined in the calculation for the "effect of wing on propeller."

(1) L_w = Scale lift - Total L_p = 3,357 - 2(1,076.4) = 1,204.2 lb

D_w = Scale drag - Total D_p = 484 - 2(-841.0) = 2,166.0

Scale lift and drag are read as the total lift and drag of system. Therefore, total propeller lift and drag (twice the propeller lift and drag calculated in preceding section) are subtracted from the scale reading to obtain lift and drag on the wing.

$(D_i)_w = D_w = 2{,}166.0$ lb

$(D_i/L)_w = 2{,}166.0/1{,}204.2 \approx 1.80$

(2) $w_h = -\sqrt{\frac{L_w}{n\rho(A_m)_w}} = -\sqrt{\frac{602.1}{2(0.002338)(235)}} = -23.4$ ft/sec

Only one wing element is analyzed because of symmetry. Each element is considered to contribute one-half of the total lift and one-half of the total momentum area.

(3) $V/w_h = 69.1/-23.4 = -2.95$

(4) $w_o/w_h = 0.458$ (from fig. 6, ref. 4)

(5) $V/w_o = \frac{V/w_h}{w_o/w_h} = -2.95/0.458 = -6.44$

(6) $\chi = 77.8^\circ$ (from fig. 7, ref. 4)

(7) $\delta_{w,L} = -0.042$

(8) $\delta_{u,L} = 0.522$

$\delta_{w,D} = -0.500$

$\delta_{u,D} = 0.102$

(9) $M_w/M_t = \frac{(A_m)_w}{A_t}\Big/V/w_o = 235/1{,}607/-6.44 = -0.02267$

(10) $M_u/M_t = (M_w/M_t)(D_i/L)_w = (-0.02267)(1.80) = -0.04081$

(11) $\Delta w_L/V = \delta_{w,L}(M_w/M_t) = (-0.042)(-0.02267) = 0.00095$

(12) $\Delta u_L/V = \delta_{u,L}(M_w/M_t) = (0.522)(-0.02267) = -0.01183$

(13) $\Delta w_D/V = \delta_{w,D}(M_u/M_t) = (-0.500)(-0.04081) = 0.02041$

(14) $\Delta u_D/V = \delta_{u,D}(M_u/M_t) = (0.102)(-0.04081) = -0.00416$

(15) $(\Delta w/V)_{w/p} = 0.02136$

(16) $(\Delta u/V)_{w/p} = -0.01599$

} To be used for composite correction.

Effect of wing on wing on itself.- The interference effect of wing element w_1 on itself and the additional interference at w_1 due to the presence of wing element w_2 was determined. This computation is similar to the calculation for the "effect of propeller on propeller on itself" and is outlined below.

Steps (1) to (6) are the same as those for the effect of wing on propeller.

(7) $\delta_{w,L} = -0.069$

(8) $\delta_{u,L} = 0.885$

$\delta_{w,D} = -0.860$

$\delta_{u,D} = 0.190$

(9) $M_w/M_t = \dfrac{(A_m)_w}{A_t}\Big/V/w_o = 235/1,607/-6.44 = -0.02267$

(10) $M_u/M_t = \left(M_w/M_t\right)\left(D_i/L\right)_w = (-0.02267)(1.80) = -0.04081$

(11) $\Delta w_L/V = \delta_{w,L}\left(M_w/M_t\right) = (-0.069)(-0.02267) = 0.00156$

(12) $\Delta u_L/V = \delta_{u,L}\left(M_w/M_t\right) = (0.885)(-0.02267) = -0.02006$

(13) $\Delta w_D/V = \delta_{w,D}\left(M_u/M_t\right) = (-0.860)(-0.04081) = 0.03510$

(14) $\Delta u_D/V = \delta_{u,D}\left(M_u/M_t\right) = (0.190)(-0.04081) = -0.00775$

(15) $(\Delta w/V)_{w/w} = 0.3666$

(16) $(\Delta u/V)_{w/w} = -0.02781$

} To be used for composite correction.

Effect of propeller on wing.- There is additional interference at wing element w_1 because of the presence of propeller element p_1. This interference is determined in the calculation for the "effect of propeller on wing."

Steps (1) to (6) are the same as those for the effect of propeller on propeller on itself.

(7) $\delta_{w,L} = -0.240$

(8) $\delta_{u,L} = 0.561$

$\delta_{w,D} = -0.620$

$\delta_{u,D} = 0.181$

} From charts prepared by using reference 5.

(9) $M_w/M_t = \dfrac{(A_m)_p/A_t}{V/w_o} = \dfrac{71/1,607}{-2.10} = -0.02104$

(10) $M_u/M_t = M_w/M_t\left(D_i/L\right)_p = (-0.02104)(-0.78) = 0.01641$

(11) $\Delta w_L/V = \delta_{w,L}\left(M_w/M_t\right) = (-0.240)(-0.02104) = 0.00505$

(12) $\Delta u_L/V = \delta_{u,L}\left(M_w/M_t\right) = (0.561)(-0.02104) = -0.01180$

(13) $\Delta w_D/V = \delta_{w,D}\left(M_u/M_t\right) = (-0.620)(0.01641) = -0.01017$

(14) $\Delta u_D/V = \delta_{u,D}\left(M_u/M_t\right) = (0.181)(0.01641) = 0.00297$

(15) $(\Delta w/V)_{p/w} = -0.00512$

(16) $(\Delta u/V)_{p/w} = -0.00883$

} To be used for composite correction.

Angle-of-attack correction.- Having determined the interference velocities at propeller element p_1 and wing element w_1, the angle-of-attack correction can be determined. Step (17) of the procedure shows that $\Delta\alpha$ can be determined from the relationship $\Delta\alpha = \dfrac{\Delta w/V}{1 + \Delta u/V}$. The values $\Delta w/V$ and $\Delta u/V$ for this computation are the sums of the individual lifting element contributions to $\Delta w/V$ and $\Delta u/V$ and are called $(\Delta w/V)_m$ and $(\Delta u/V)_m$.

(1) $(\Delta w/V)_m = (\Delta w/V)_{p/p} + (\Delta w/V)_{p/w} + (\Delta w/V)_{w/w} + (\Delta w/V)_{w/p}$

$= -0.01178 - 0.00512 + 0.03666 + 0.02136$

$= 0.04112$

(2) $(\Delta u/V)_m = (\Delta u/V)_{p/p} + (\Delta u/V)_{p/w} + (\Delta u/V)_{w/w} + (\Delta u/V)_{w/p}$

$= -0.01490 - 0.00883 - 0.02781 - 0.01599$

$= -0.06753$

(3) $\Delta\alpha = \tan^{-1} \frac{(\Delta w/V)_m}{1 + (\Delta u/V)_m} = \tan^{-1} \frac{0.04112}{0.93247} = \tan^{-1} 0.04409 = 2.5^\circ$

This angle-of-attack correction is to be used in determining the corrected lift and drag.

Effect of propeller on rake.- Next the interference effects of the wing element w_1 and propeller element p_1 on the rake were determined to be used to determine the corrected dynamic pressure q_c. The interference effects of the propeller on the rake were determined as follows:

Steps (1) to (6) are the same as those for the effect of propeller on propeller on itself.

(7) $\delta_{w,L} = -0.057$

(8) $\delta_{u,L} = 0.292$

$\delta_{w,D} = -0.267$

$\delta_{u,D} = 0.208$

} From charts prepared by using reference 5.

(9) $M_w/M_t = \frac{(A_m)_p/A_t}{V/w_o} = \frac{71/1,607}{-2.10} = -0.02104$

(10) $M_u/M_t = M_w/M_t(D_i/L)_p = (-0.02104)(-0.78) = 0.01641$

(11) $\Delta w_L/V = \delta_{w,L}(M_w/M_t) = (-0.057)(-0.02104) = 0.00120$

(12) $\Delta u_L/V = \delta_{u,L}(M_w/M_t) = (0.292)(-0.02104) = -0.00614$

(13) $\Delta w_D/V = \delta_{w,D}(M_u/M_t) = (-0.267)(0.01641) = -0.00438$

(14) $\Delta u_D/V = \delta_{u,D}(M_u/M_t) = (0.208)(0.01641) = 0.00341$

(15) $(\Delta w/V)_{p/r} = -0.00318$

(16) $(\Delta u/V)_{p/r} = -0.00273$

} To be used for rake contribution.

Effect of wing on rake.- Likewise, the interference effects of the wing on the rake were determined as follows:

Steps (1) to (6) are the same as those for the effect of wing on propeller.

(7) $\delta_{w,L} = -0.040$

(8) $\delta_{u,L} = 0.239$

$\delta_{w,D} = -0.240$

$\delta_{u,D} = 0.156$

(9) $M_w/M_t = \dfrac{(A_m)_w}{A_t}\Big/V/w_o = 235/1,607/-6.44 = -0.02267$

(10) $M_u/M_t = (M_w/M_t)(D_i/L)_w = (-0.02267)(1.80) = -0.04081$

(11) $\Delta w_L/V = \delta_{w,L}(M_w/M_t) = (-0.040)(-0.02267) = 0.00091$

(12) $\Delta u_L/V = \delta_{u,L}(M_w/M_t) = (0.239)(-0.02267) = -0.00542$

(13) $\Delta w_D/V = \delta_{w,D}(M_u/M_t) = (-0.240)(-0.04081) = 0.00979$

(14) $\Delta u_D/V = \delta_{u,D}(M_u/M_t) = (0.156)(-0.04081) = -0.00637$

(15) $(\Delta w/V)_{w/r} = 0.01070$

(16) $(\Delta u/V)_{w/r} = -0.01179$

} To be used for rake contribution.

Total rake contribution.- The total rake contribution is then the sum of the interference velocities determined for the effects of the wing and propeller on the rake.

(1) $(\Delta w/V)_r = (\Delta w/V)_{p/r} + (\Delta w/V)_{w/r} = -0.00318 + 0.01070 = 0.00752$

(2) $(\Delta u/V)_r = (\Delta u/V)_{p/r} + (\Delta u/V)_{w/r} = -0.00273 - 0.01179 = -0.01452$

Dynamic-pressure correction.- The dynamic-pressure correction was determined as follows:

(1) $(\Delta w/V)_{eff} = (\Delta w/V)_m - (\Delta w/V)_r = 0.04112 - 0.00752 = 0.03360$

(2) $(\Delta u/V)_{eff} = (\Delta u/V)_m - (\Delta u/V)_r = -0.06753 + 0.01452 = -0.05301$

(3) $q_c/q_t = \left[1 + (\Delta u/V)_{eff}\right]^2 + \left[(\Delta w/V)_{eff}\right]^2 = (0.94699)^2 + (0.03360)^2 = 0.89792$

(4) $q_c = (q_c/q_t)q_t = (0.89792)(5.58) = 5.01$

Lift and lift coefficient correction.- The lift and lift coefficient correction were determined as follows:

(1) $L_c = L \cos \Delta\alpha - D \sin \Delta\alpha = (3,357)(0.99905) - (484)(0.04362) = 3,332.7$

(2) $C_{L,c} = \dfrac{L_c}{q_c S} = 3,332.7/(5.01)(118.2) = 5.628$

Drag and drag coefficient correction.- Likewise, the drag and drag coefficient correction were determined.

(1) $D_c = L \sin \Delta\alpha + D \cos \Delta\alpha = 3,357(0.04362) + 484(0.99905) = 629.97$

(2) $C_{D,c} = \frac{D_c}{q_c S} = 629.97/(5.01)(118.2) = 1.064$

Corrected angle of attack.- The corrected angle of attack includes the stream angle correction β and is determined as follows:

$$\alpha_c = \alpha + \Delta\alpha + \beta$$

$$\alpha_c = 12 + 2.5 - 0.5$$

$$\alpha_c = 14.0^\circ$$

REFERENCES

1. Pegg, Robert J.: Summary of Flight-Test Results of the VZ-2 Tilt-Wing Aircraft. NASA TN D-989, 1962.

2. Reeder, John P.: Handling Qualities Experience With Several VTOL Research Aircraft. NASA TN D-735, 1961.

3. Ward, John F.: Structural-Loads Surveys on Two Tilt-Wing VTOL Configurations. NASA TN D-729, 1961.

4. Heyson, Harry H.: Linearized Theory of Wind-Tunnel Jet-Boundary Corrections and Ground Effect for VTOL-STOL Aircraft. NASA TR R-124, 1962.

5. Heyson, Harry H.: Tables of Interference Factors for Use in Wind-Tunnel and Ground-Effect Calculations for VTOL-STOL Aircraft. Part I - Wind Tunnels Having Width-Height Ratio of 2.0. NASA TN D-933, 1962.

6. Yaggy, Paul F., and Rogallo, Vernon L.: A Wind-Tunnel Investigation of Three Propellers Through an Angle-of-Attack Range From 0° to 85°. NASA TN D-318, 1960.

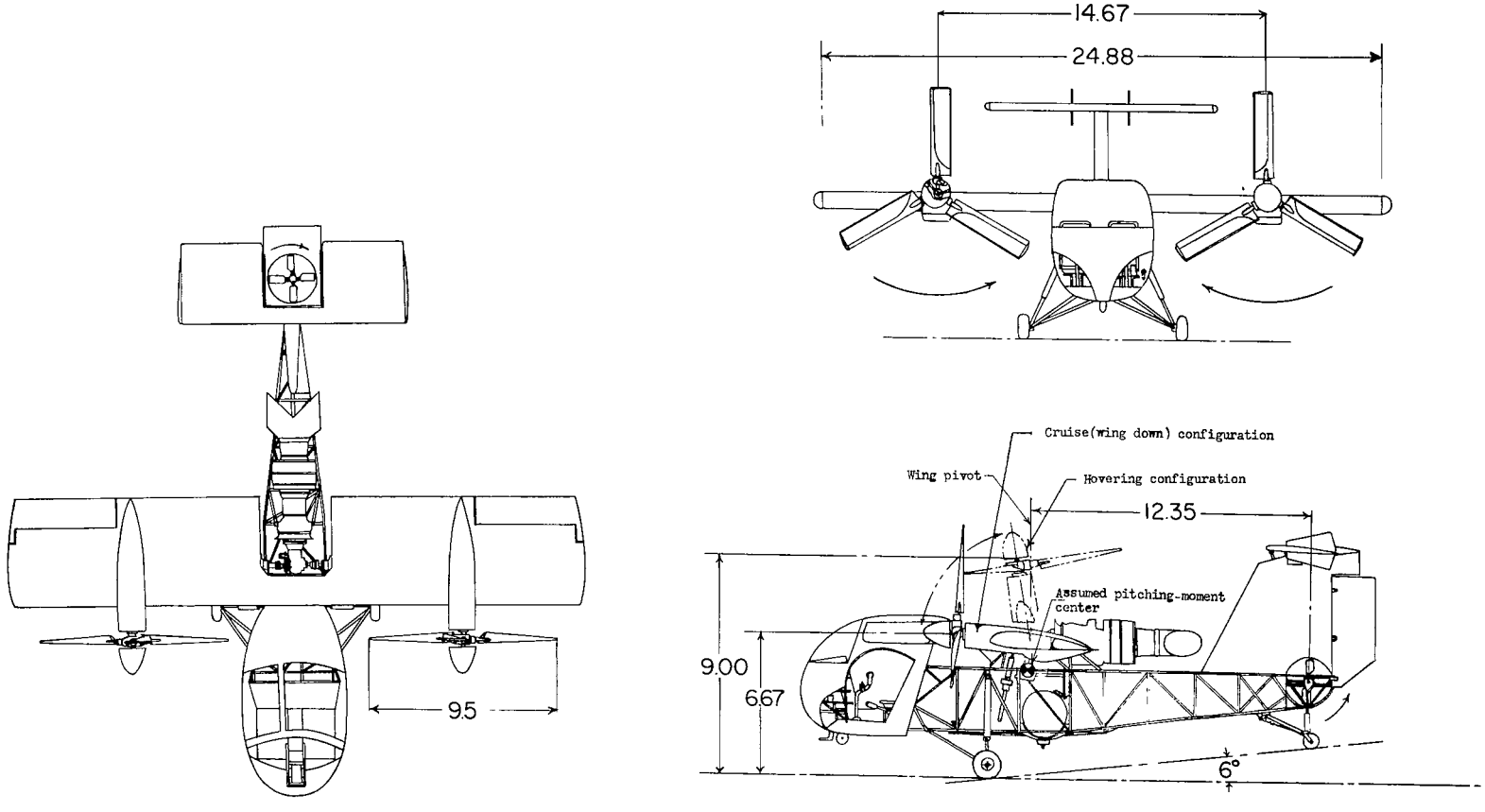

(a) Sketch of tilt-wing VTOL aircraft. All dimensions are in feet unless otherwise specified.

Figure 1.- Sketches of VZ-2 aircraft including wing modifications.

Station, in.	Wing modification coordinates, in. - Upper ordinate	Lower ordinate
0.7125	1.75	-2.28
1.425	2.378	-2.79
2.85	3.272	-3.15
4.275	3.94	-3.175
5.70	4.468	-3.09
7.125	—	-2.92
8.55	5.283	-2.715
9.975	—	-2.55
11.40	5.843	-2.43
12.825	—	-2.34
14.25	6.224	-2.268

L.E. radius, 2.828 in.

Center at (2.691 in., -0.26 in.)

(b) Airfoil section showing droop leading edge.

(c) Airfoil section showing full-span slat. Slats extend the full length of the span (excluding tips).

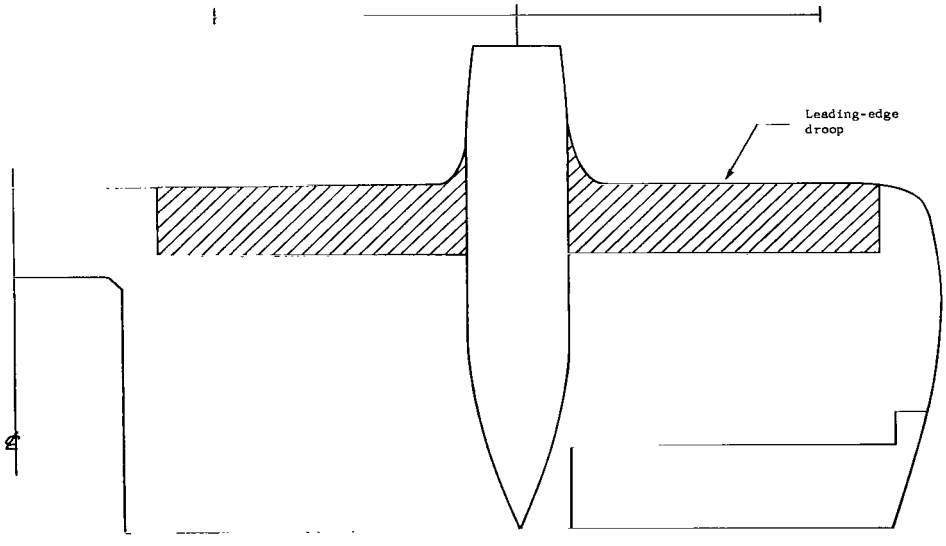

(d) Wing planform showing location of leading-edge droop. Slats not shown.

Figure 1.- Concluded.

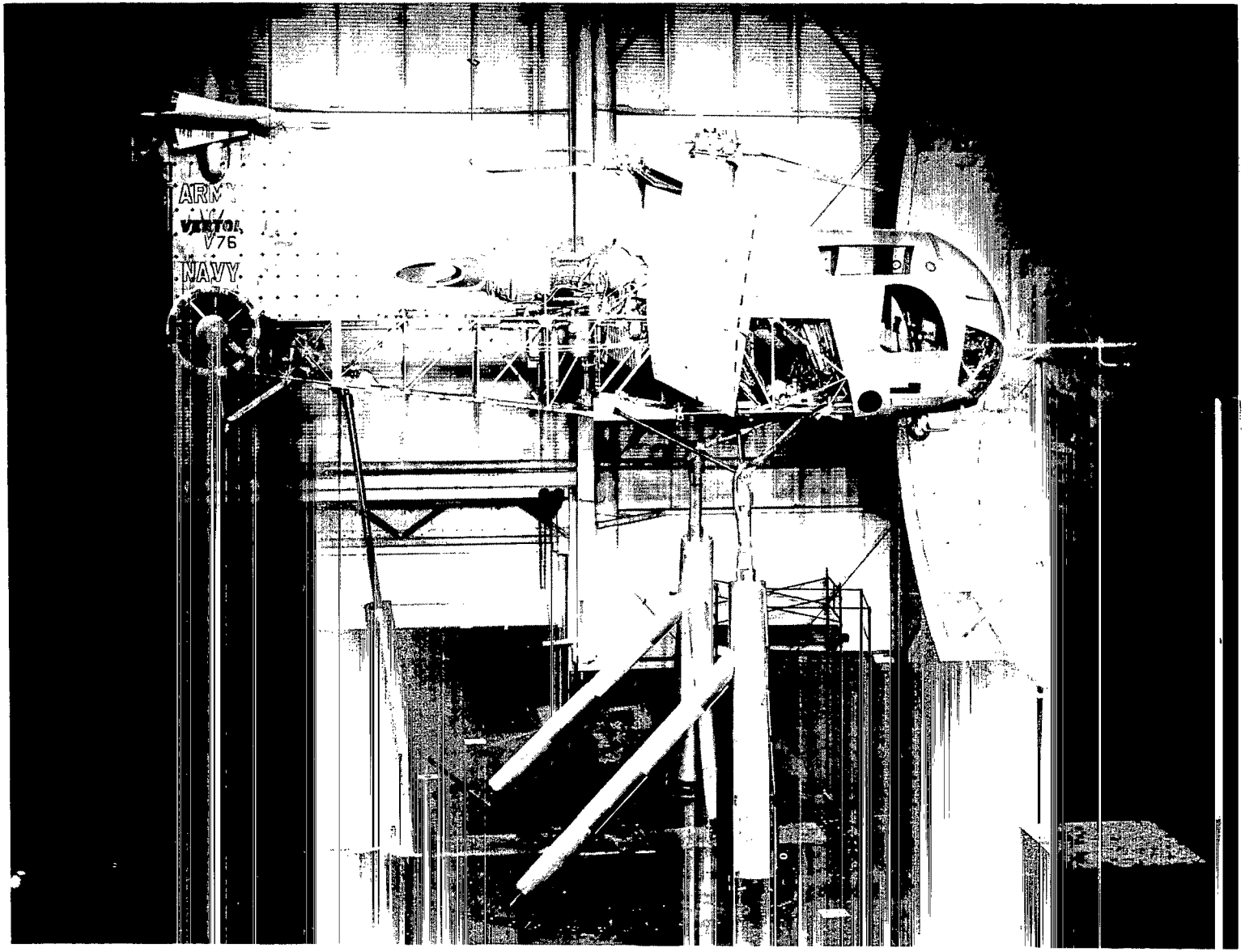

L-61-1389

Figure 2.- Photograph of the VZ-2 airplane mounted for tests in the Langley full-scale tunnel.

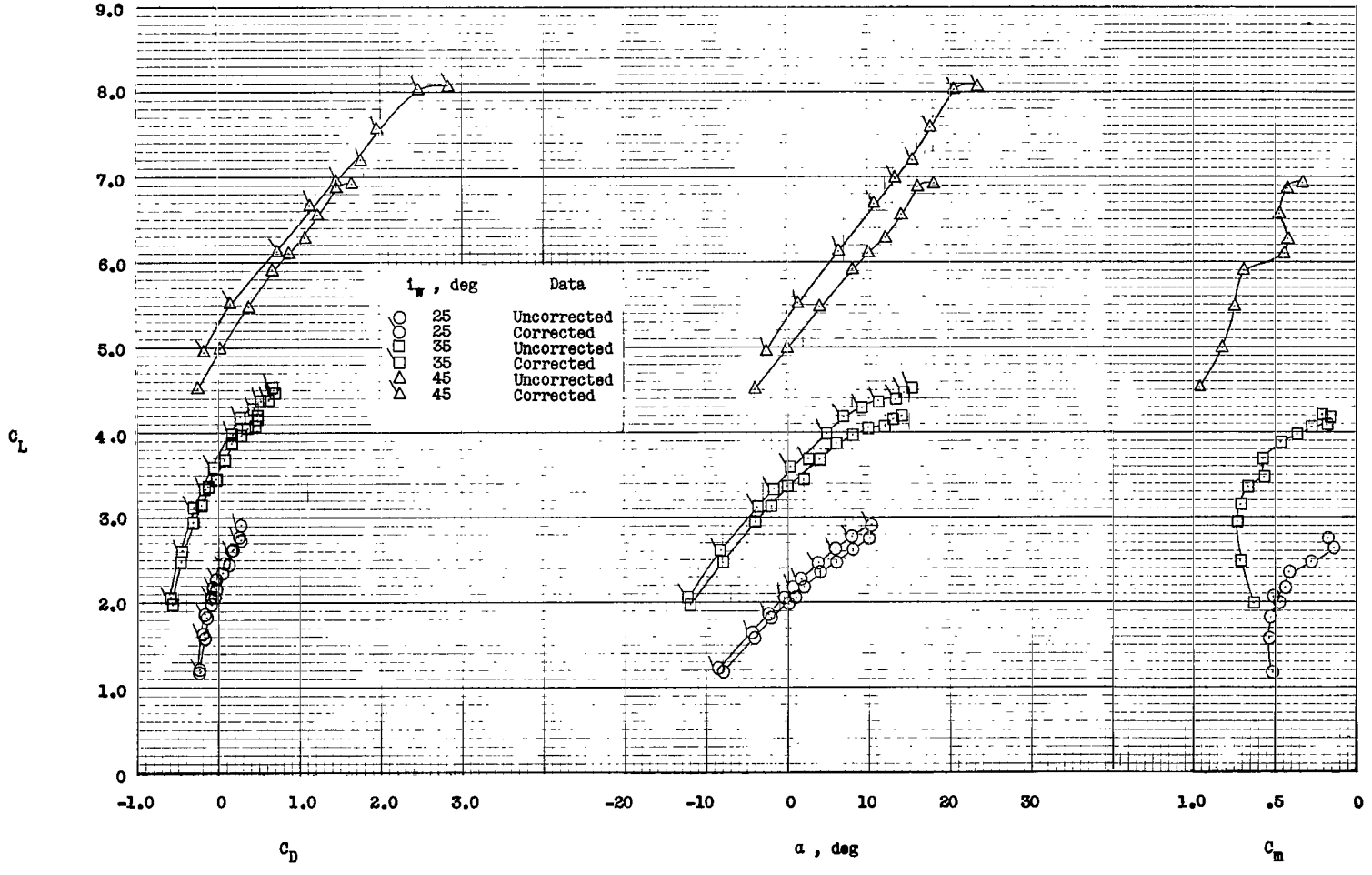

Figure 3.- Aerodynamic characteristics in the transition range for the basic wing configuration. Wing incidences of 25°, 35°, and 45°.

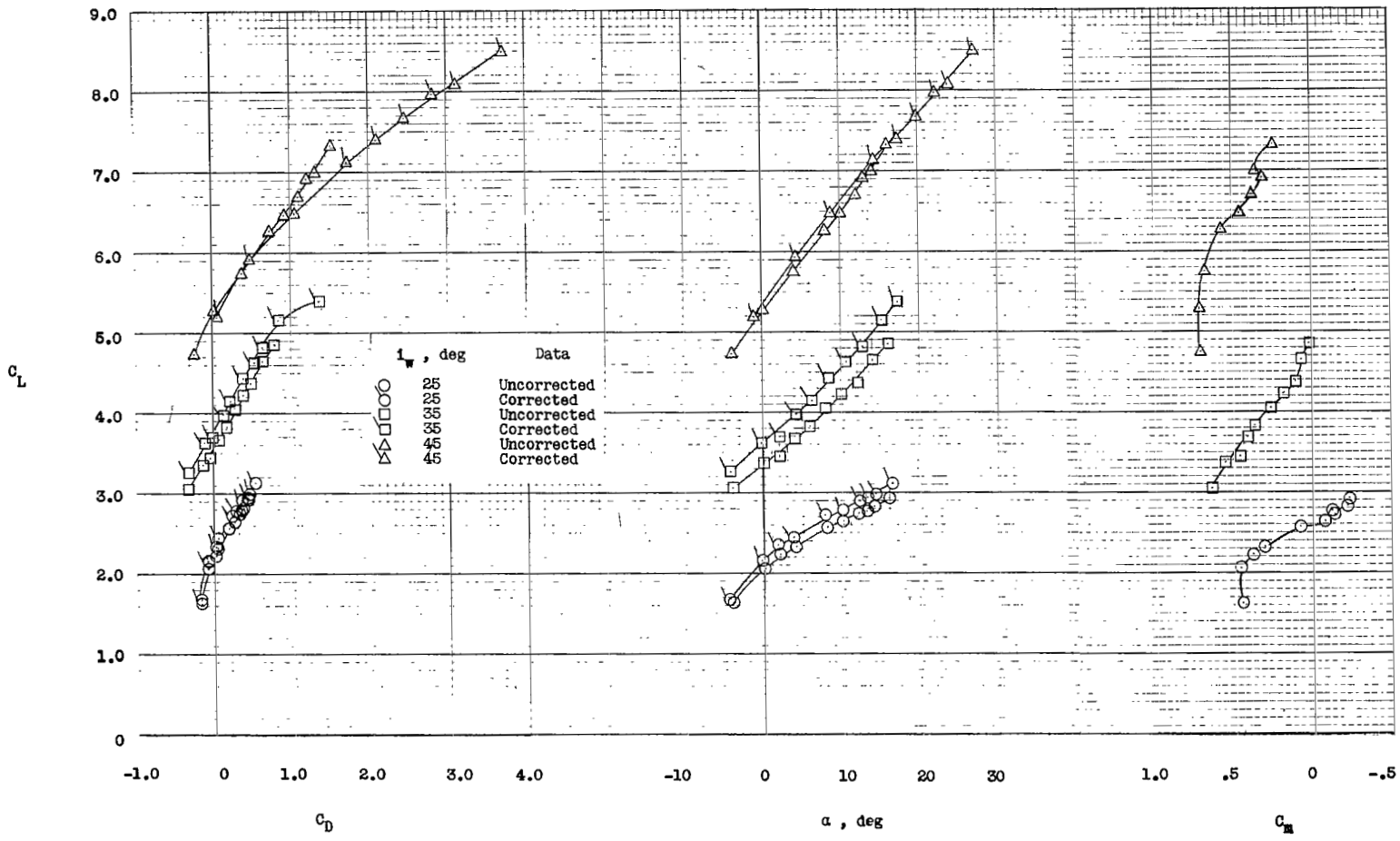

Figure 4.- Aerodynamic characteristics in the transition range for the wing configuration with a modified leading edge. Wing incidences of 25°, 35°, and 45°.

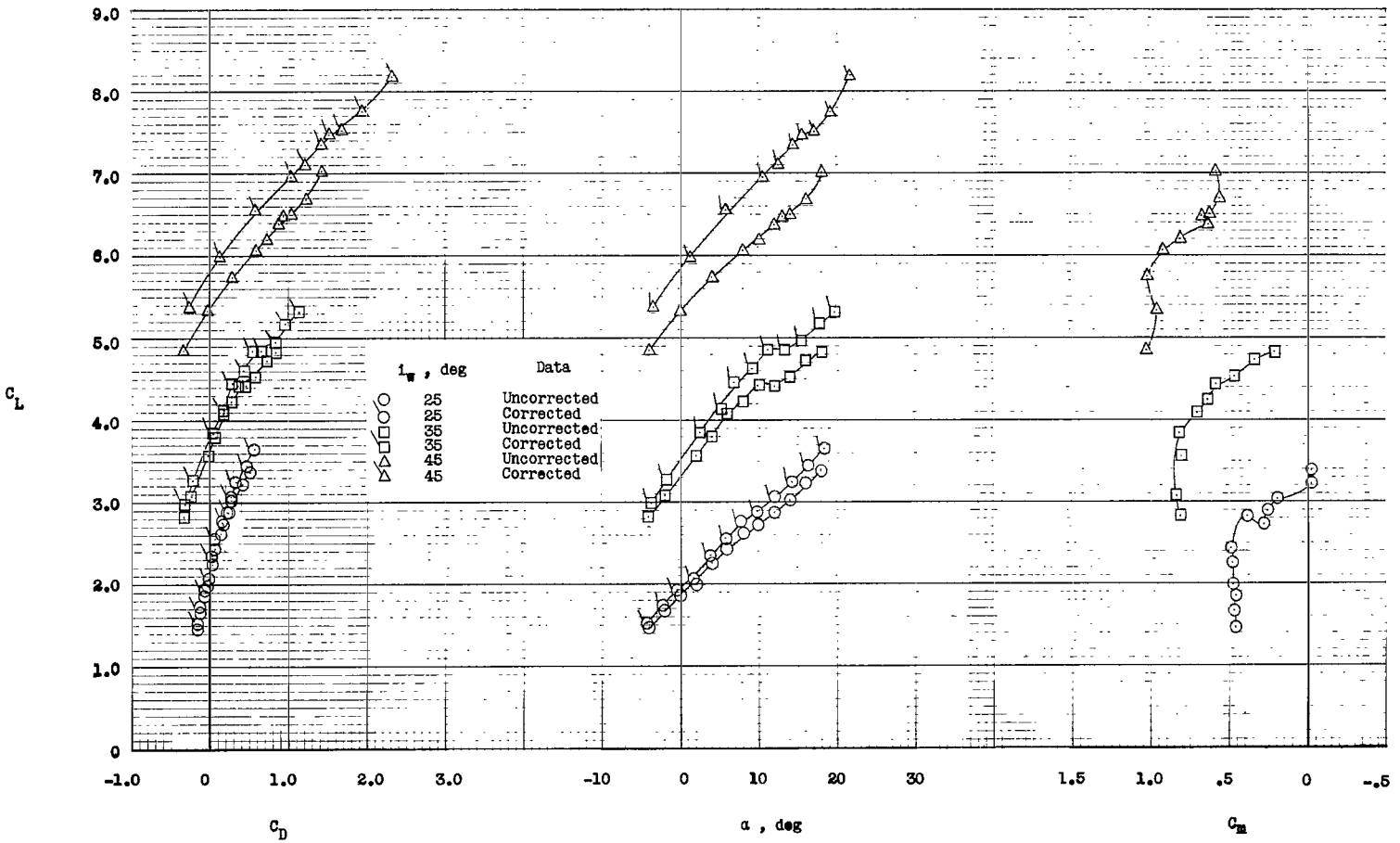

Figure 5.- Aerodynamic characteristics in the transition range for the wing configuration with full-span slats. Wing incidences of 25°, 35°, and 45°.

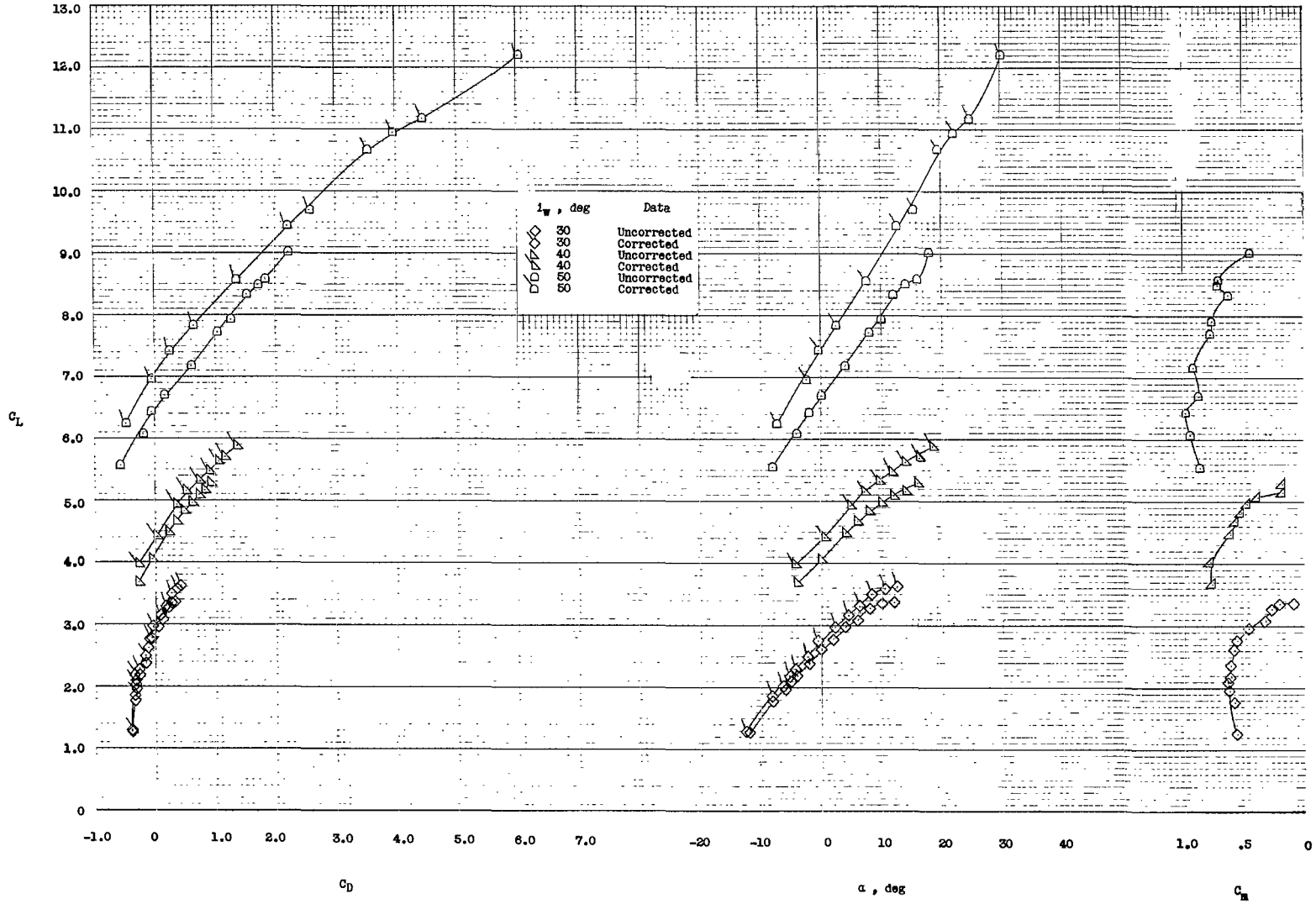

Figure 6.- Aerodynamic characteristics in the transition range for the basic wing configuration. Wing incidences of 30°, 40°, and 50°.

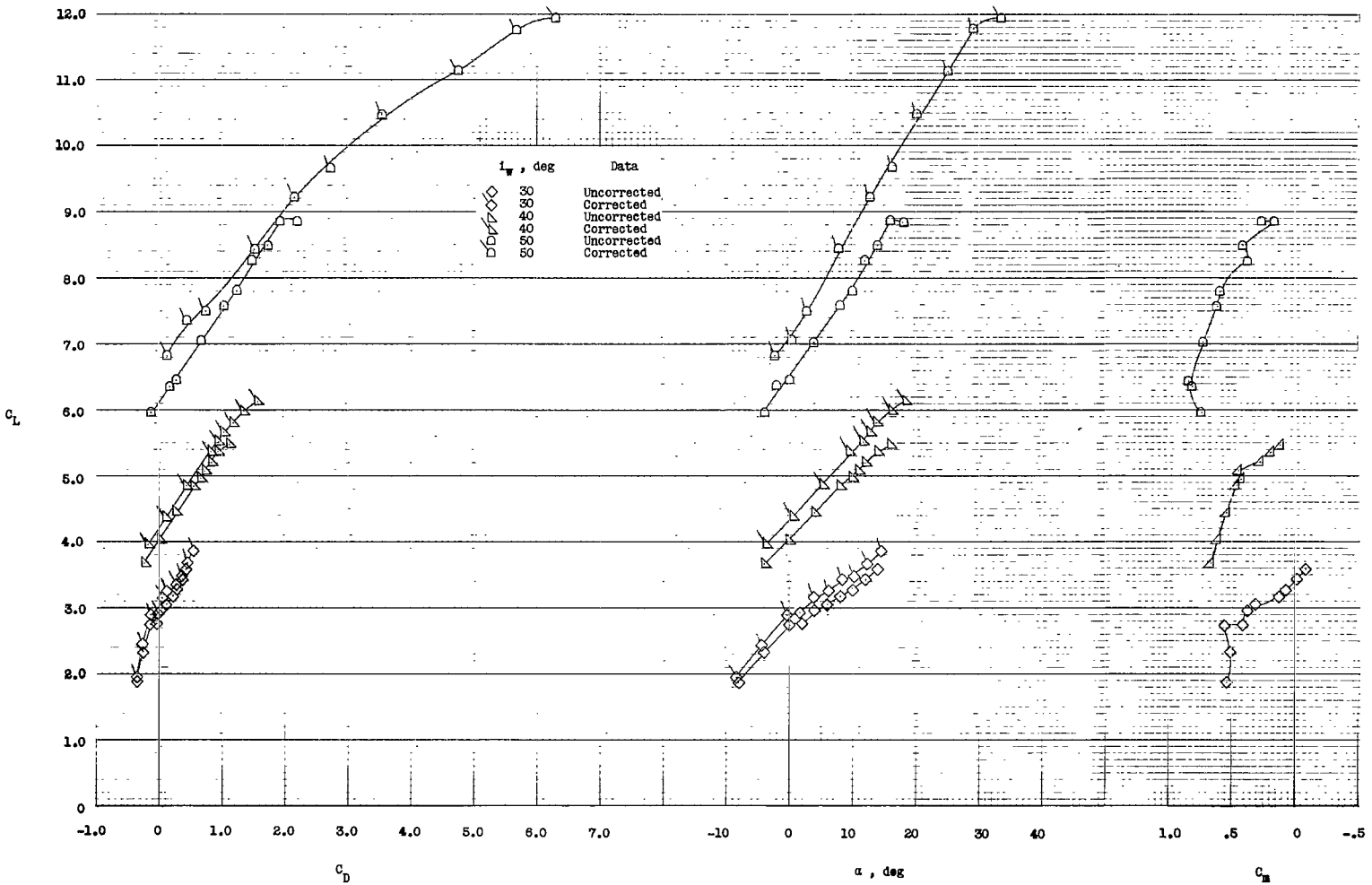

Figure 7.- Aerodynamic characteristics in the transition range for the wing configuration with a modified leading edge. Wing incidences of 30°, 40°, and 50°.

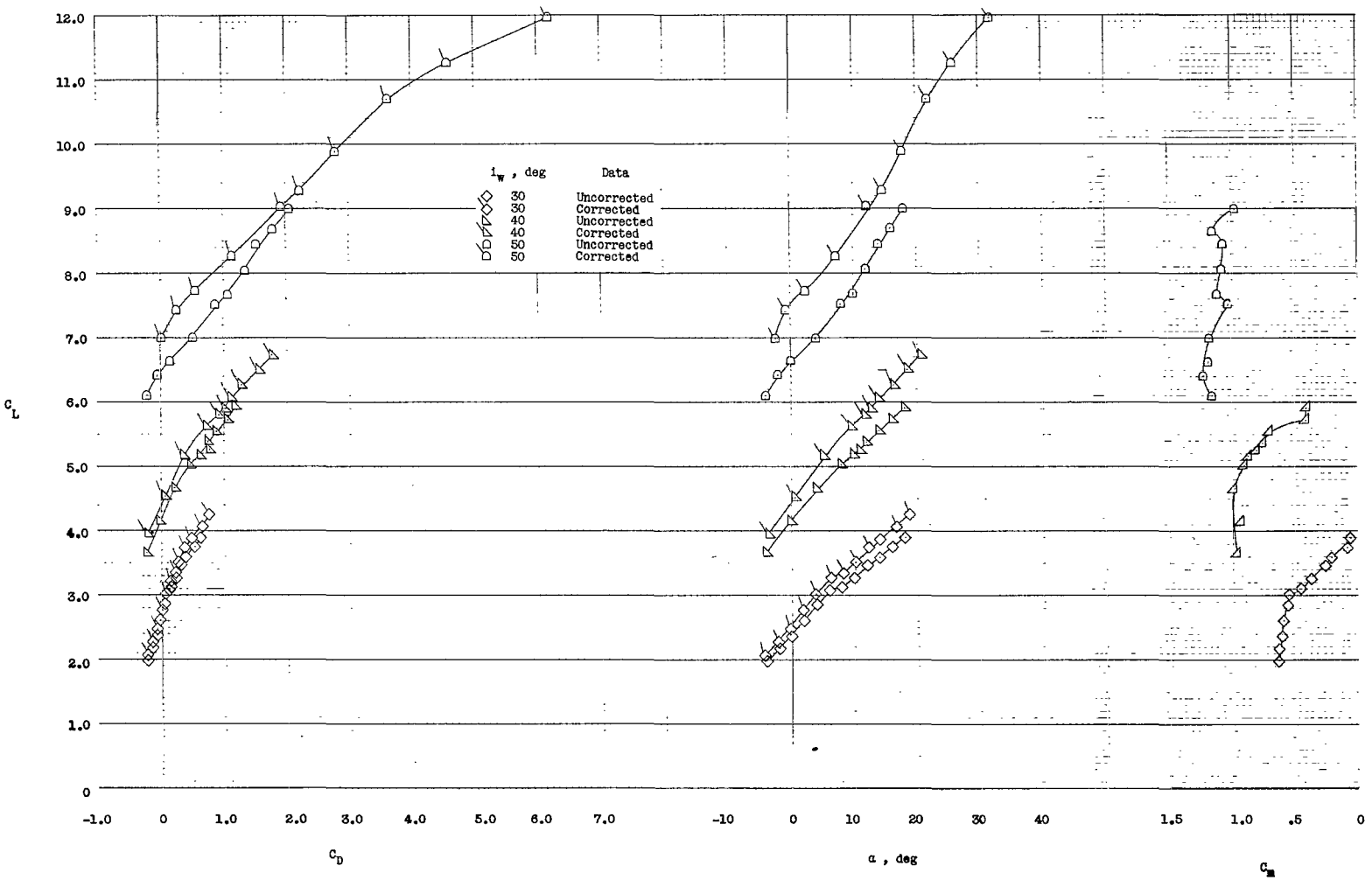

Figure 8.- Aerodynamic characteristics in the transition range for the wing configuration with full-span slats. Wing incidences of 30°, 40°, and 50°.

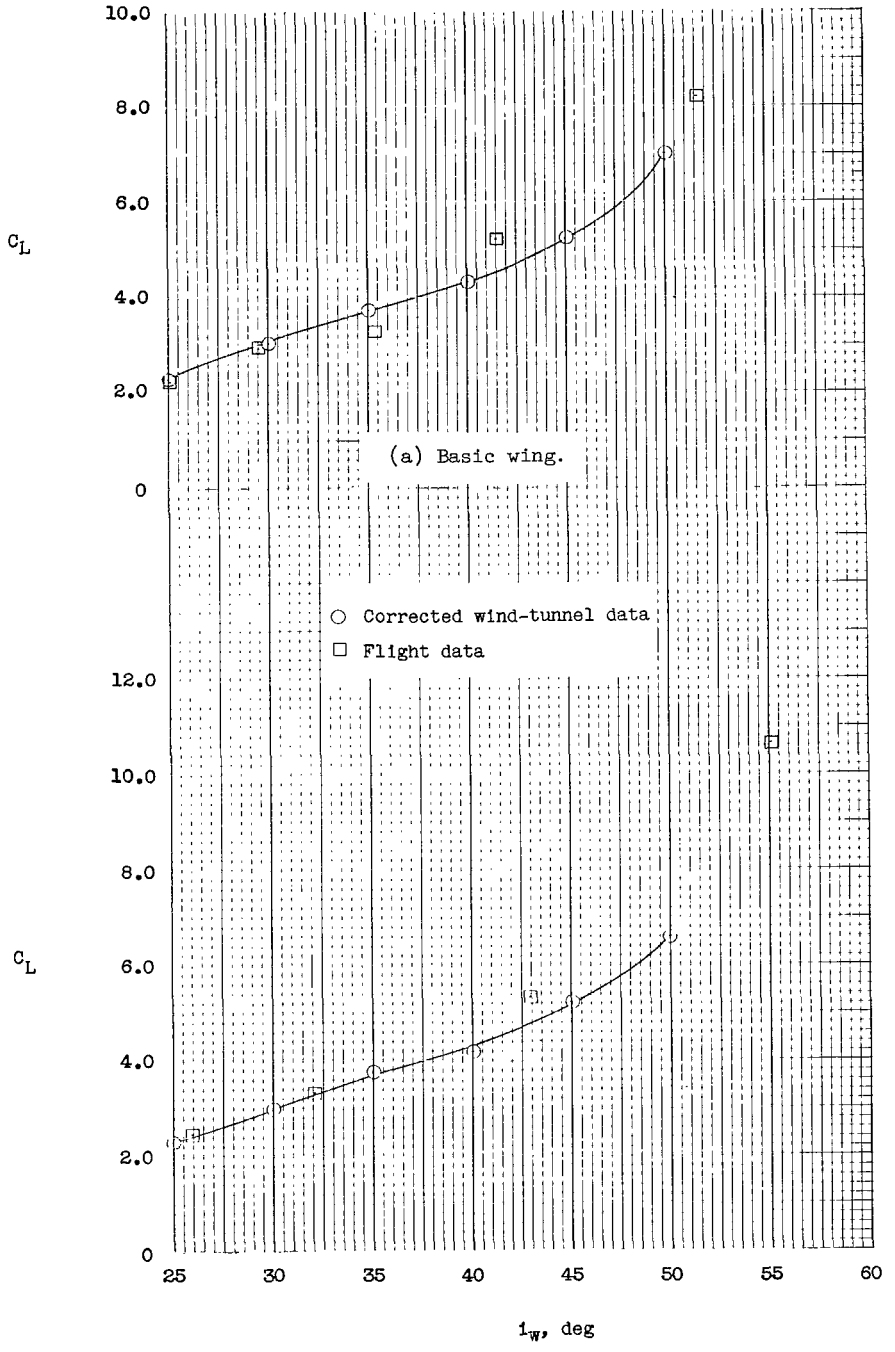

(b) Wing with modified leading edge.

Figure 9.- Correlation of corrected wind-tunnel data with flight data at trim level.

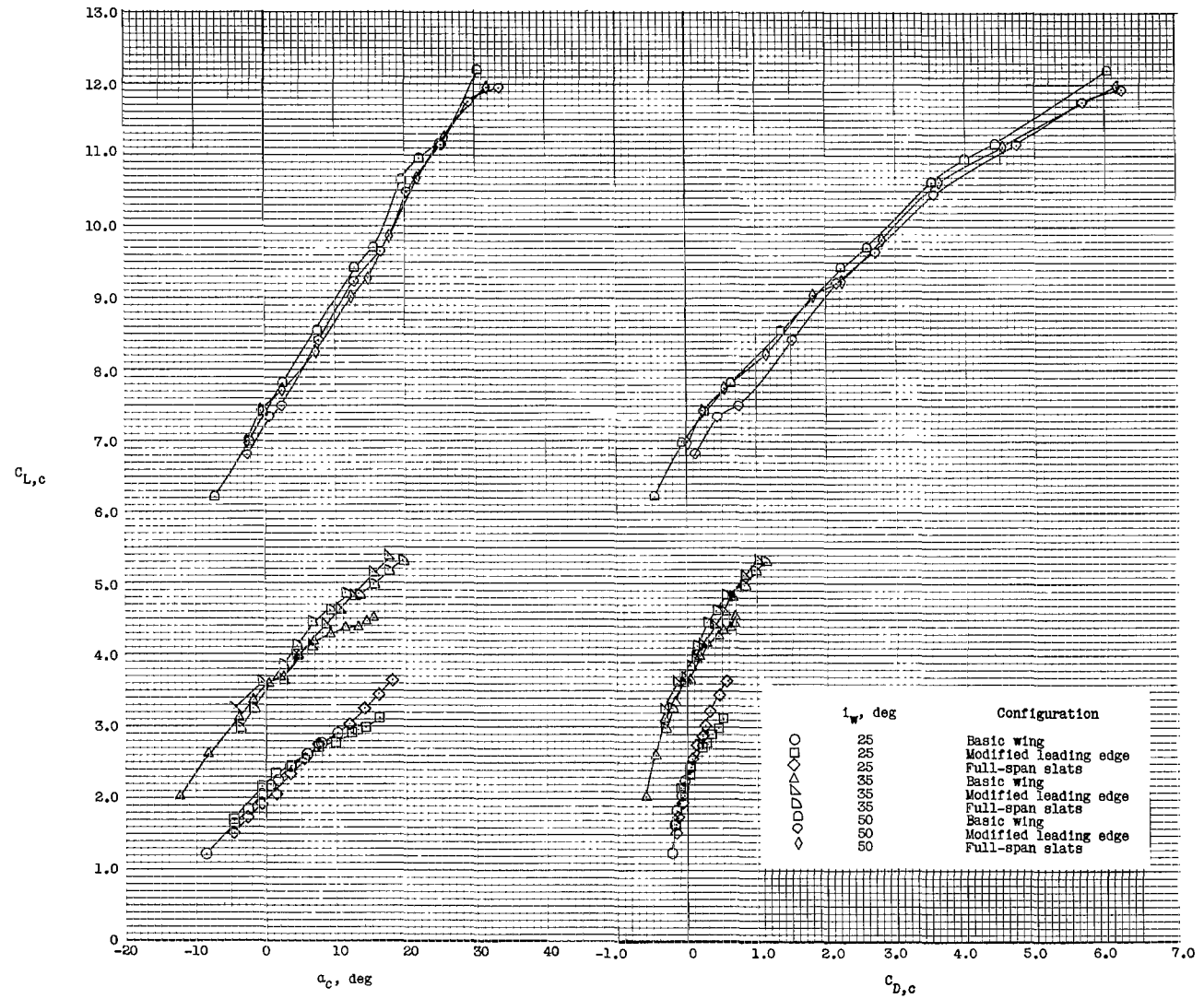

(a) Lift and drag curves for three of the wing incidences.

Figure 10.- Characteristics of lift-drag curves from present investigation and characteristics of typical lift-drag polar for a wing-propeller combination.

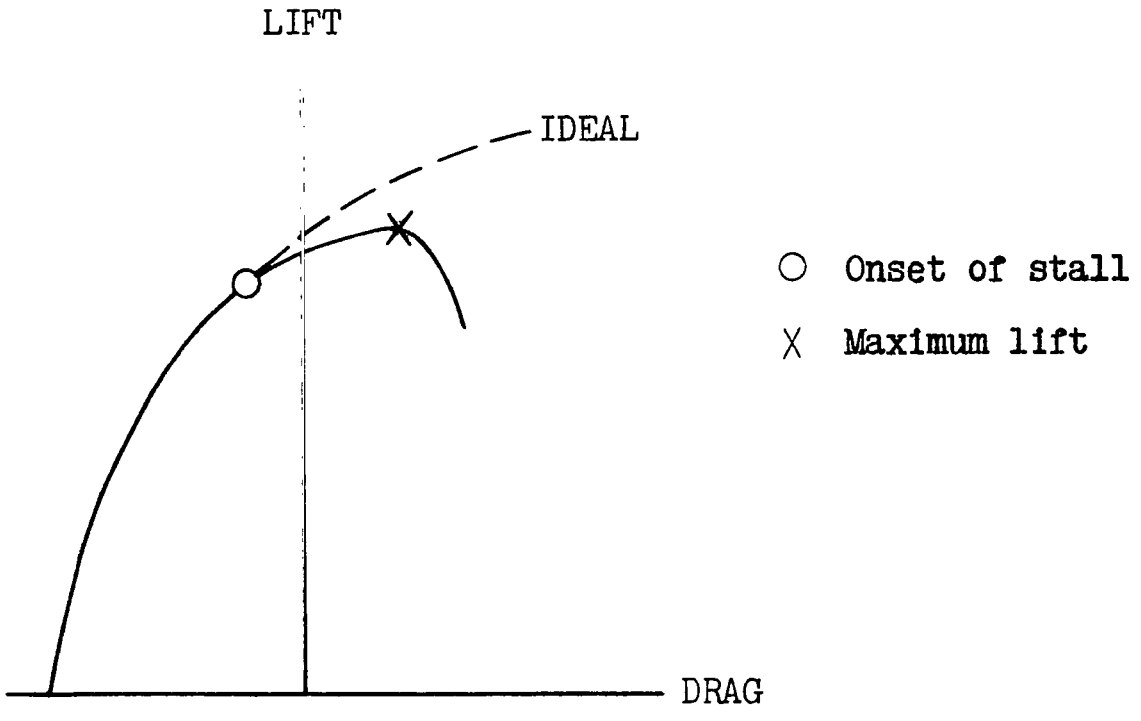

(b) Typical lift-drag polar for a wing-propeller combination.

Figure 10.- Concluded.

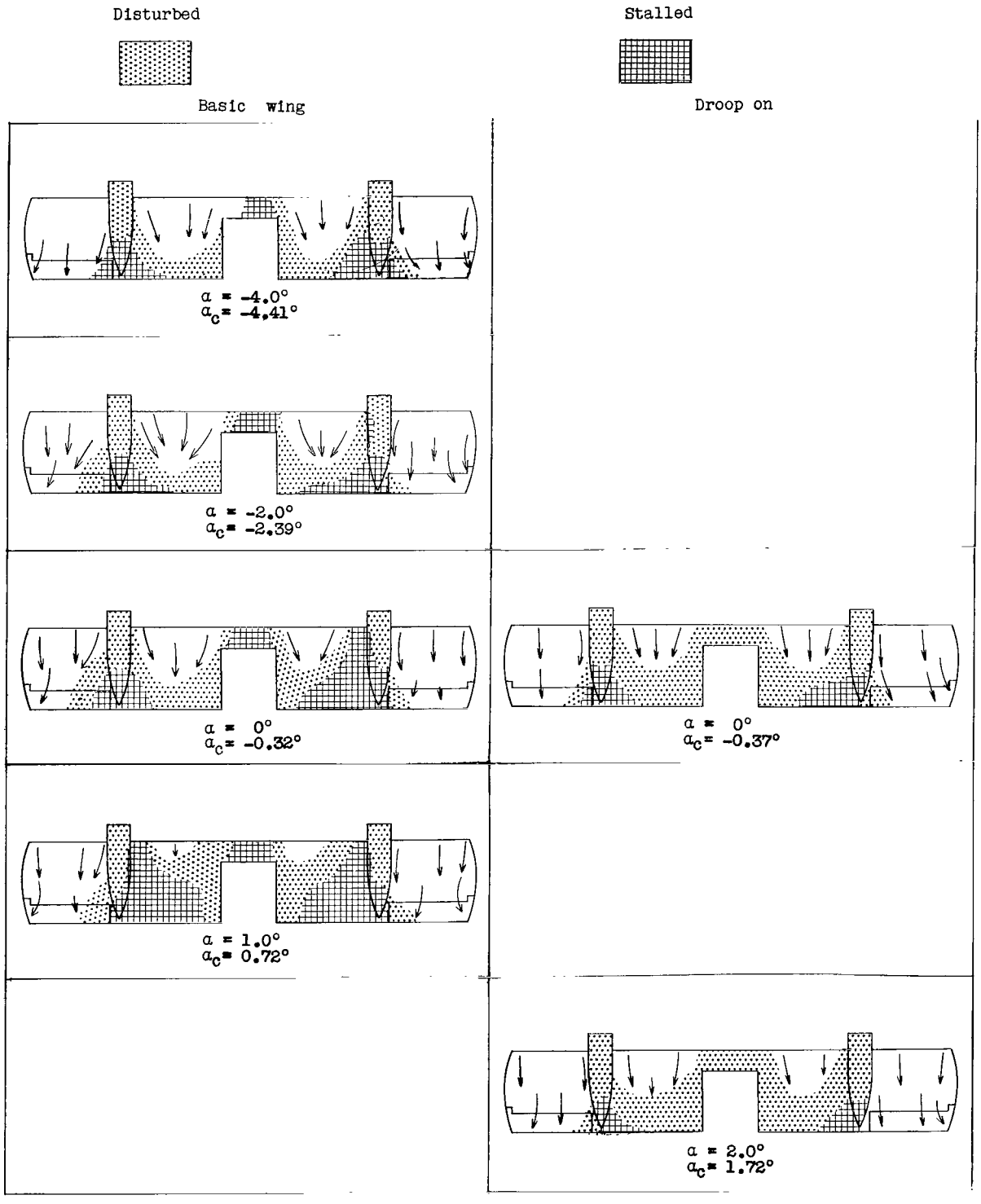

Figure 11.- Stall diagrams for the basic wing and the wing with a modified leading edge (droop on) at $i_w = 25°$.

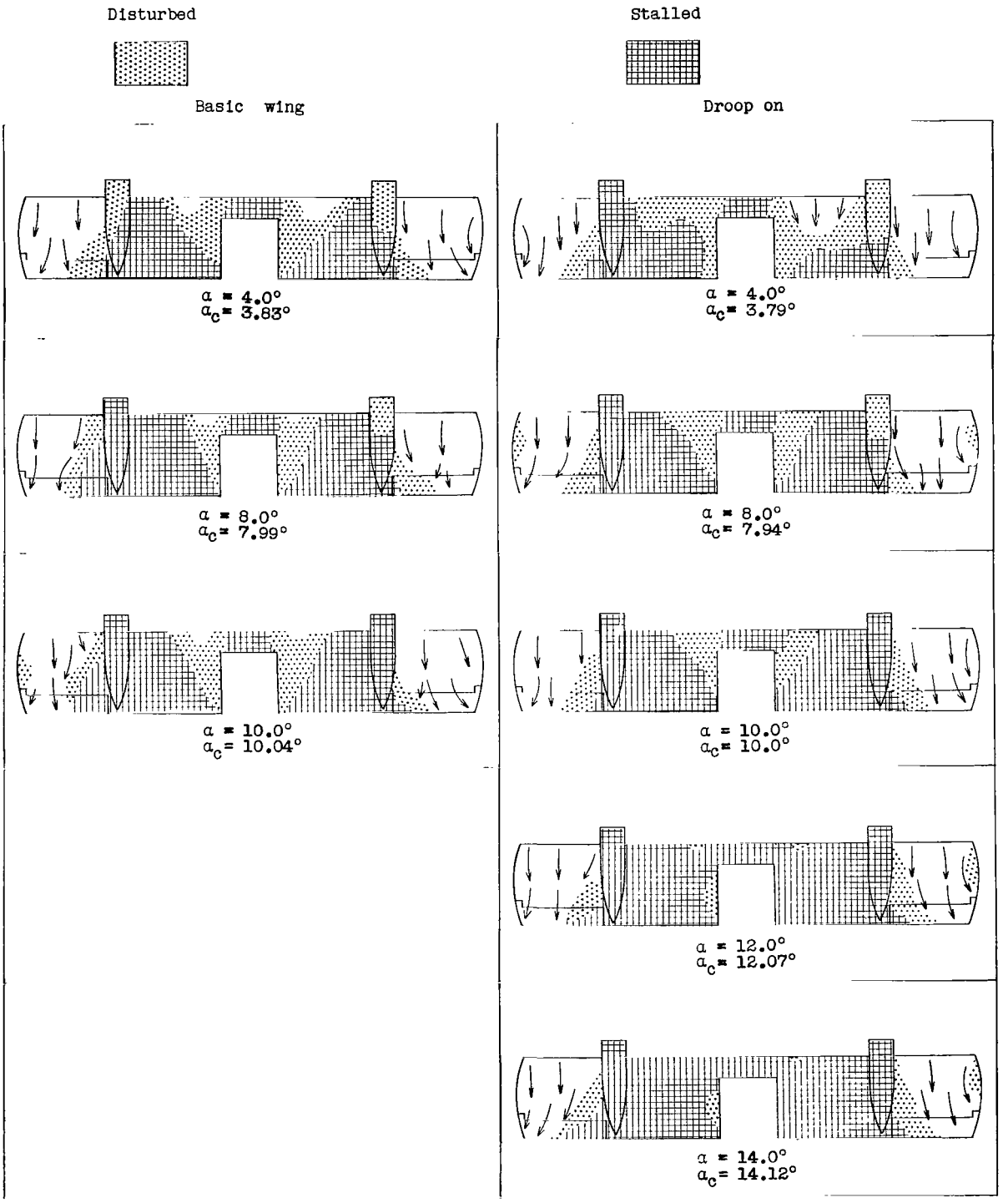

Figure 11.- Concluded.

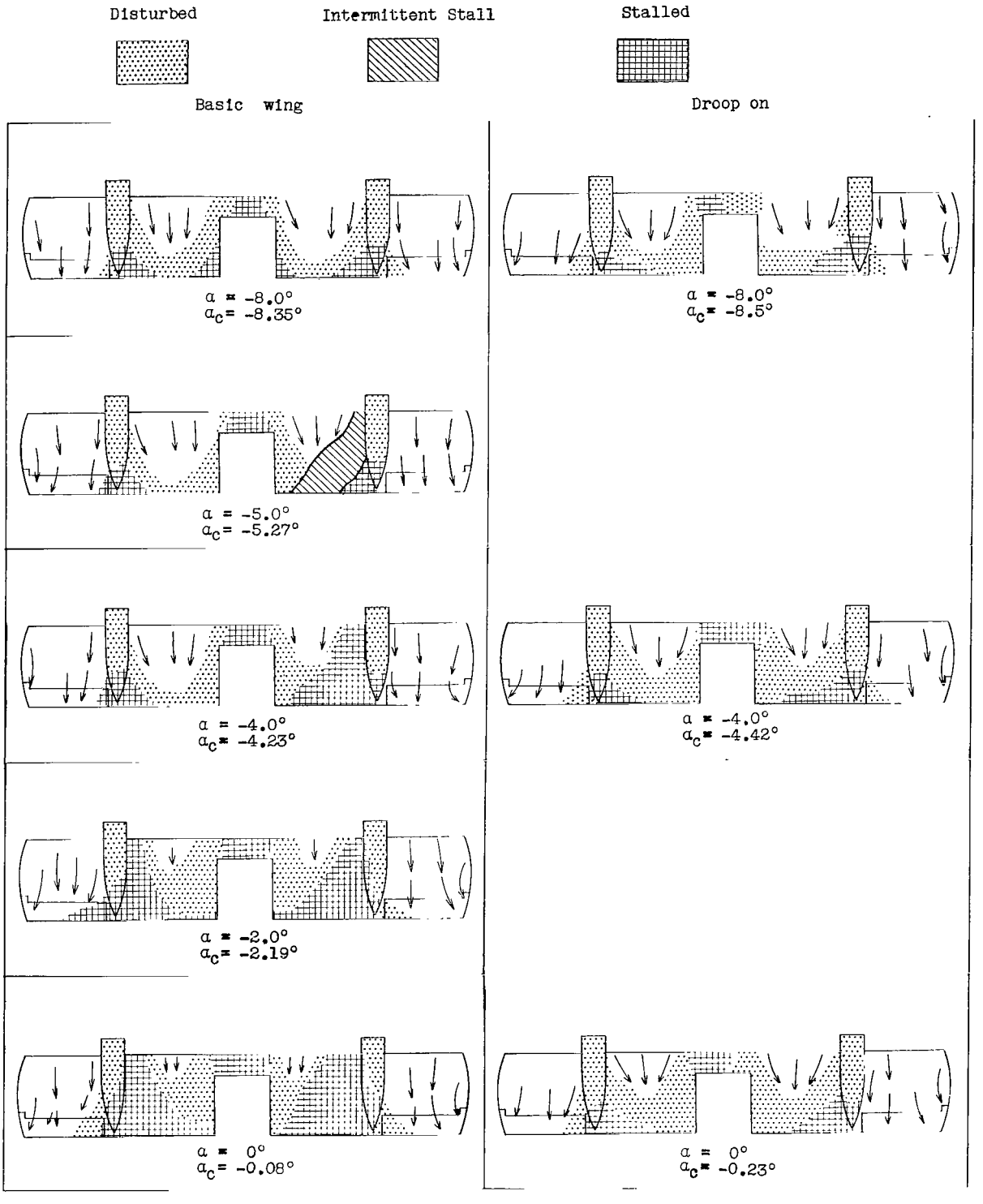

Figure 12.- Stall diagrams for the basic wing and the wing with a modified leading edge (droop on) at $i_w = 30°$.

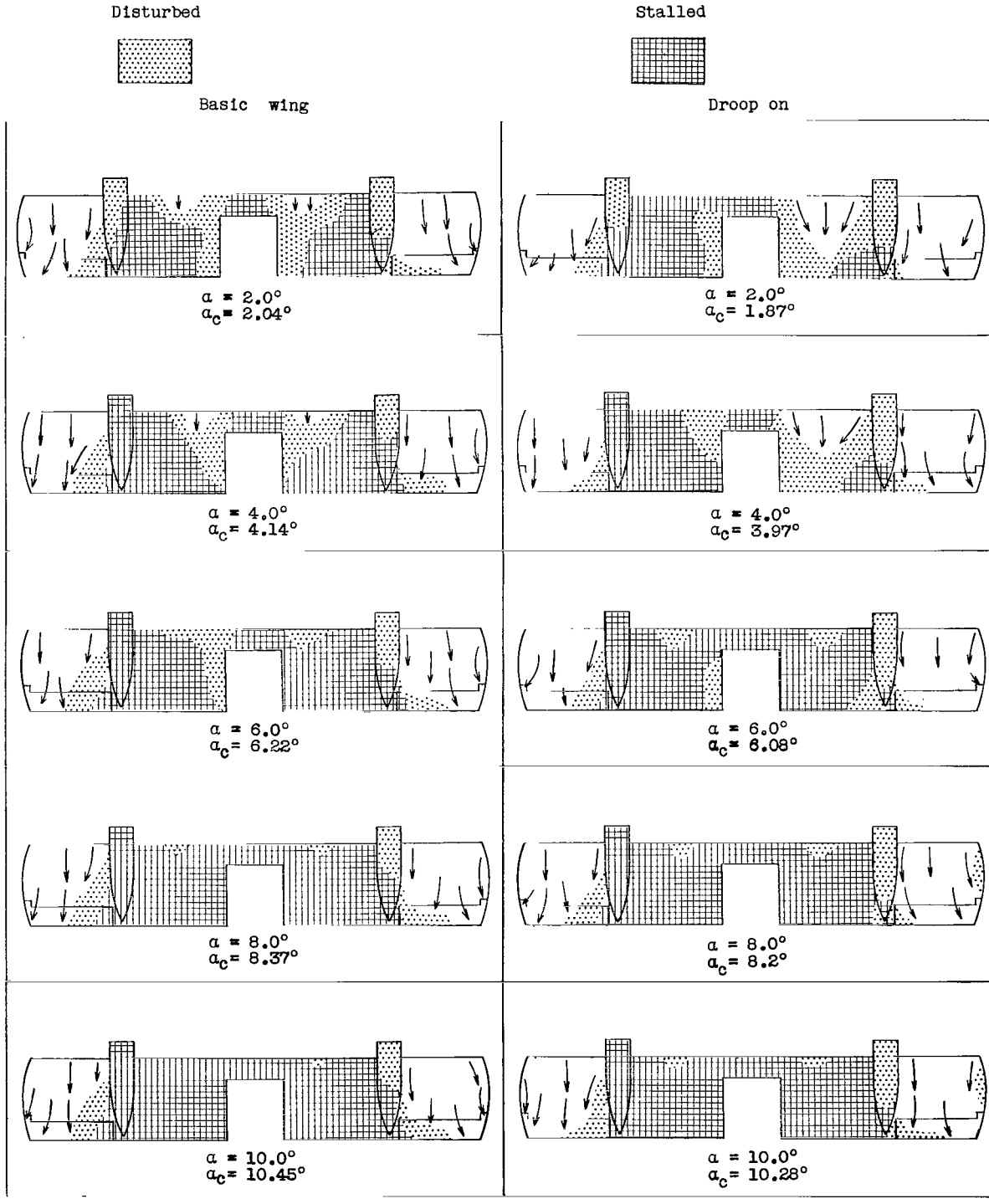

Figure 12.- Concluded.

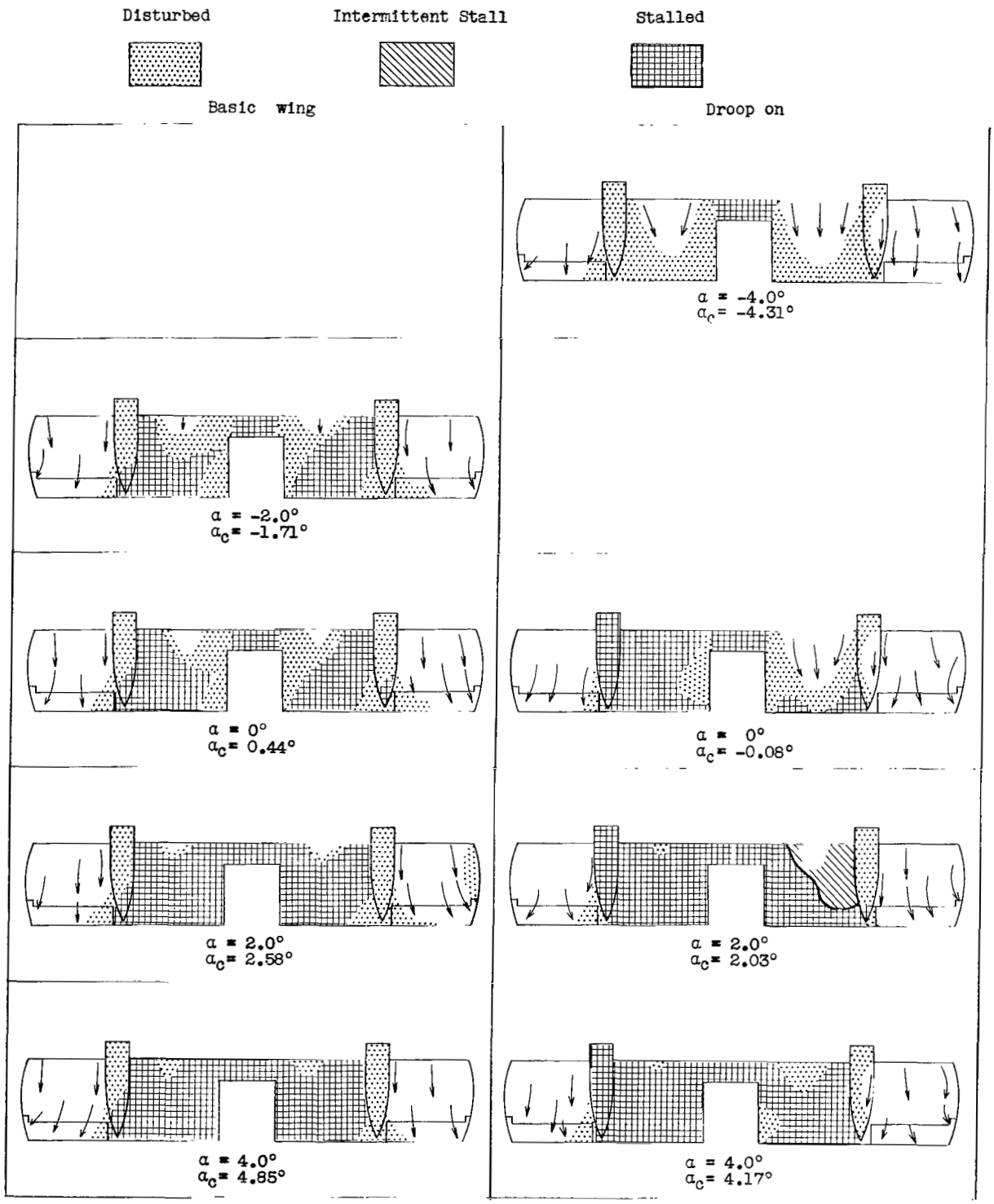

Figure 13.- Stall diagrams for the basic wing and the wing with a modified leading edge (droop on) at $i_w = 35°$.

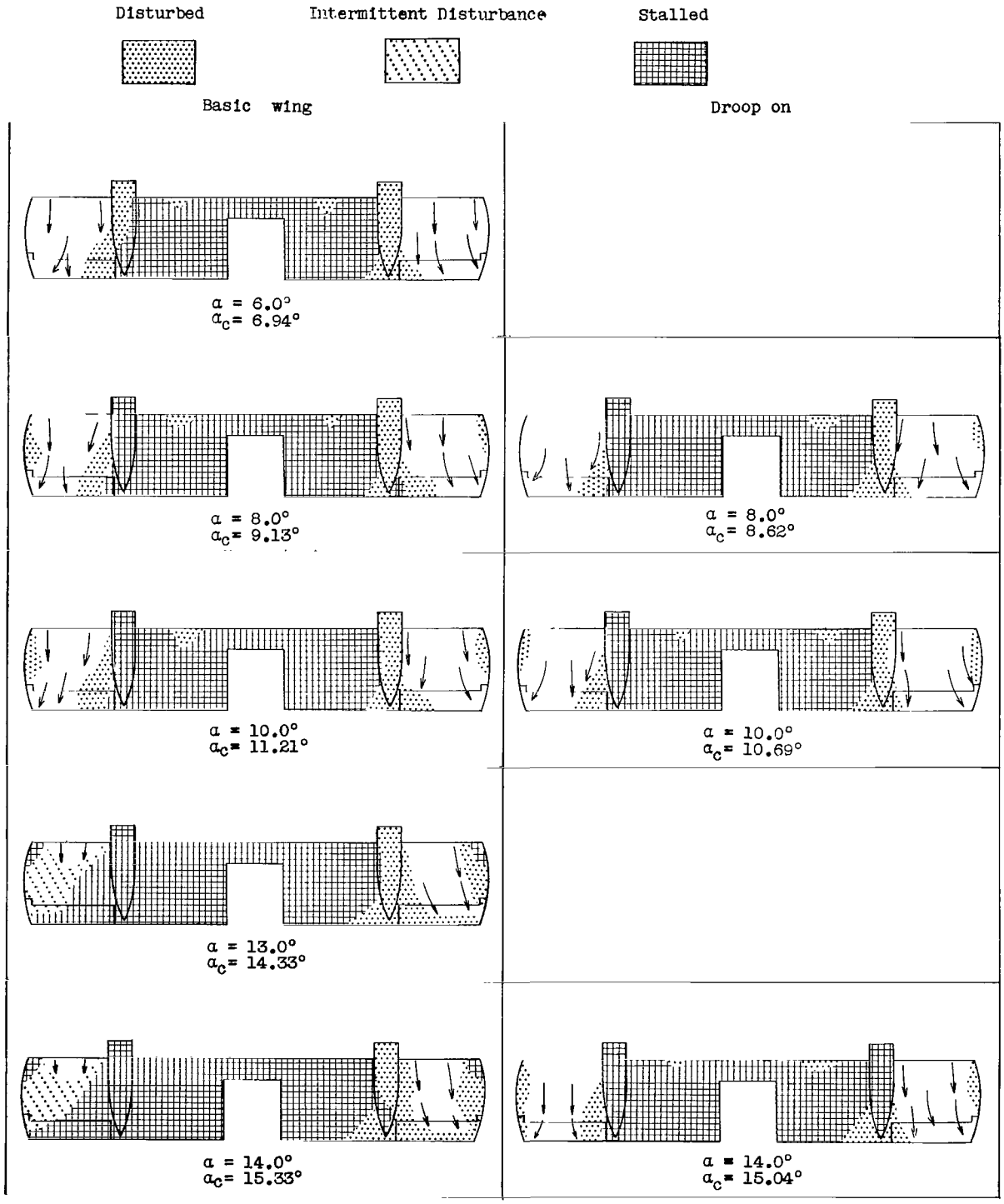

Figure 13.- Concluded.

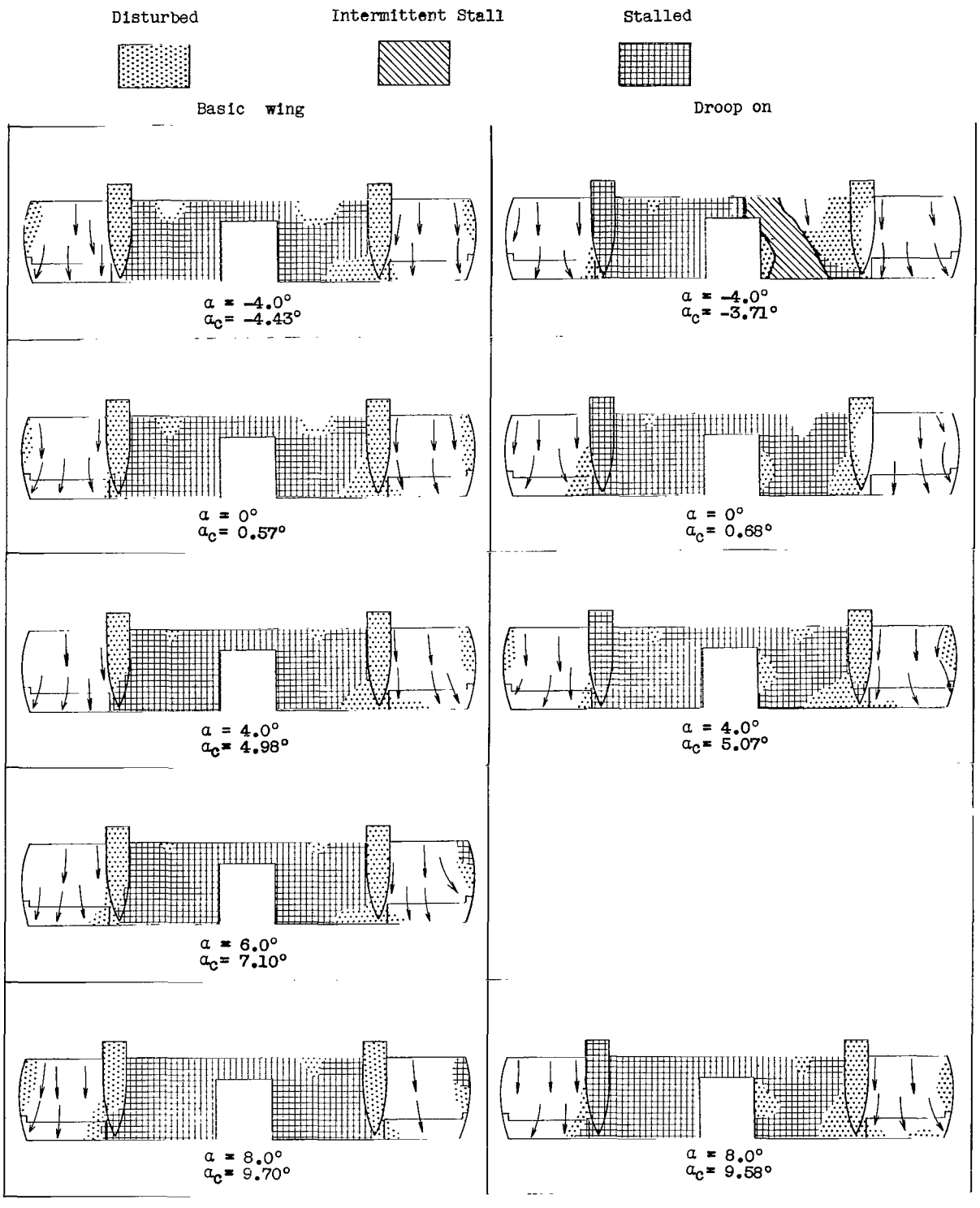

Figure 14.- Stall diagrams for the basic wing and the wing with a modified leading edge (droop on) at $i_w = 40°$.

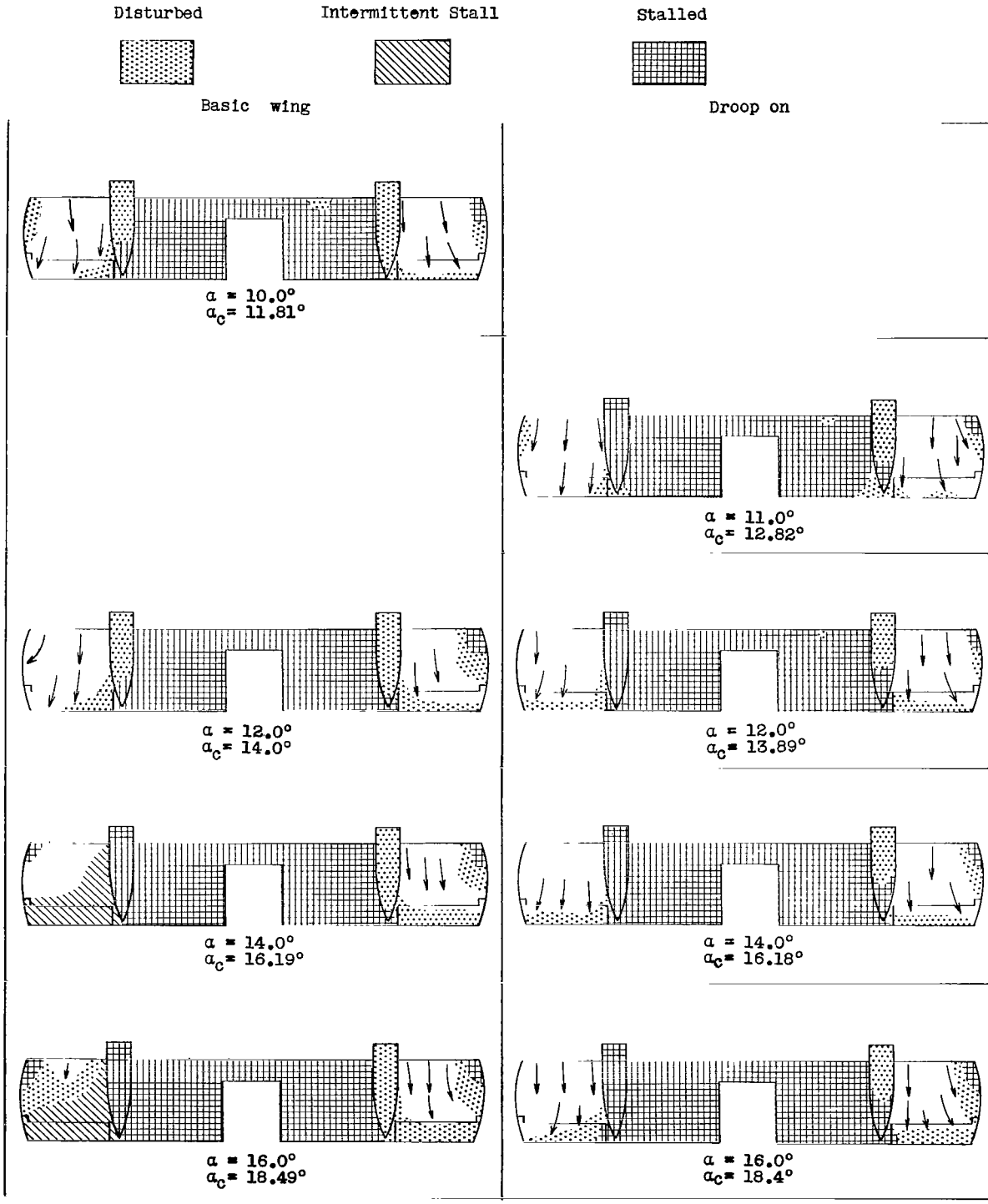

Figure 14.- Concluded.

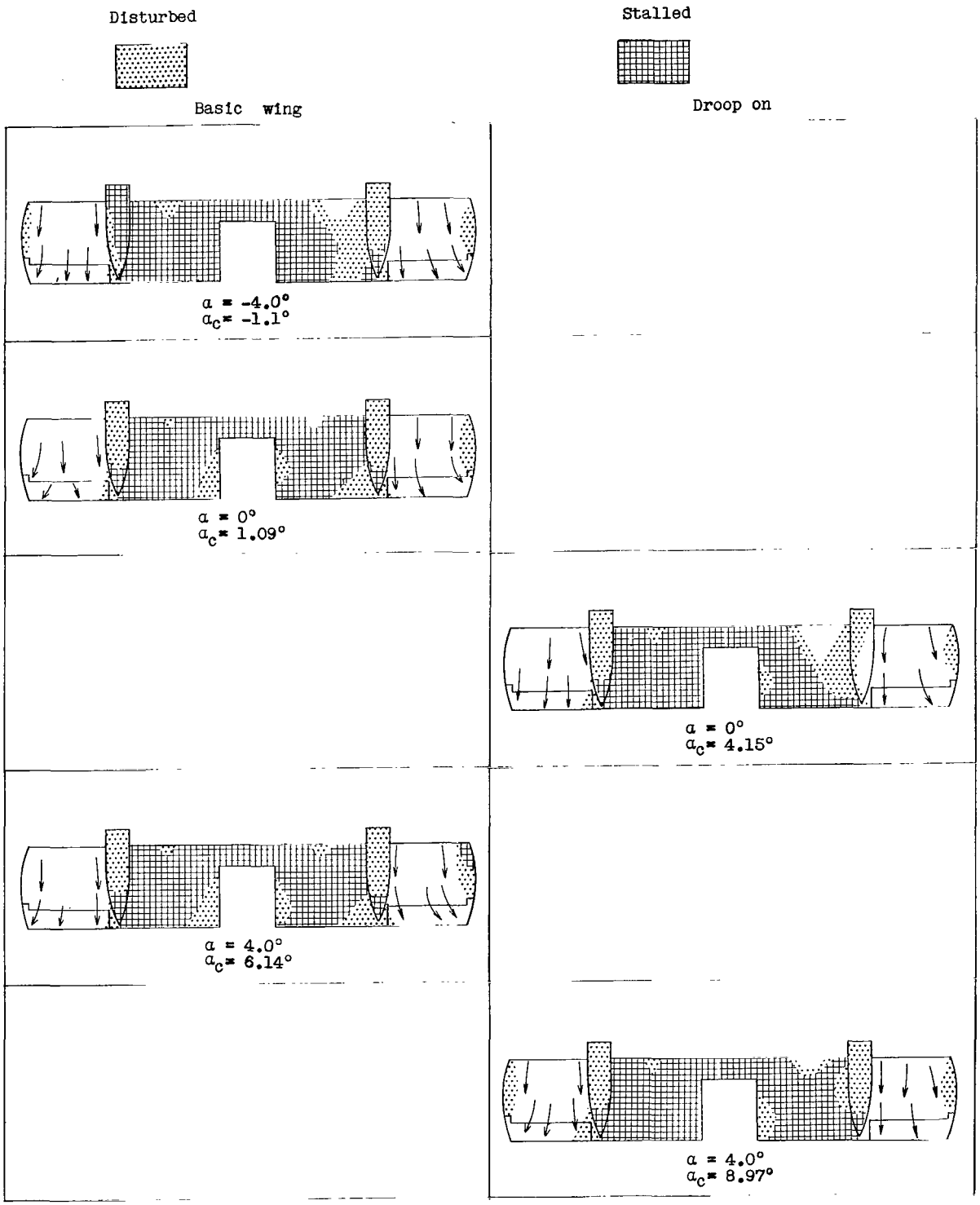

Figure 15.- Stall diagrams for the basic wing and the wing with a modified leading edge (droop on) at $i_w = 45°$.

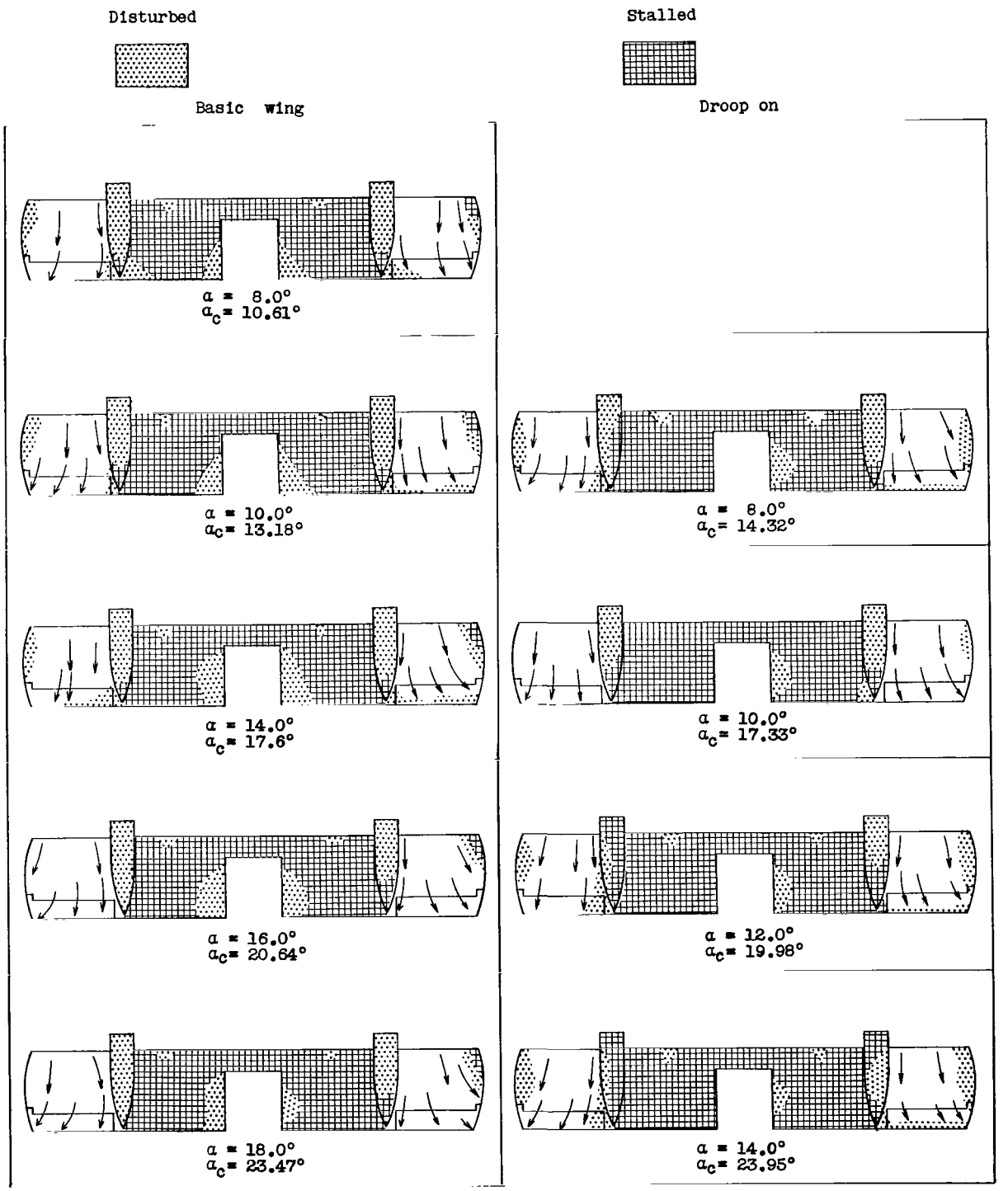

Figure 15.- Concluded.

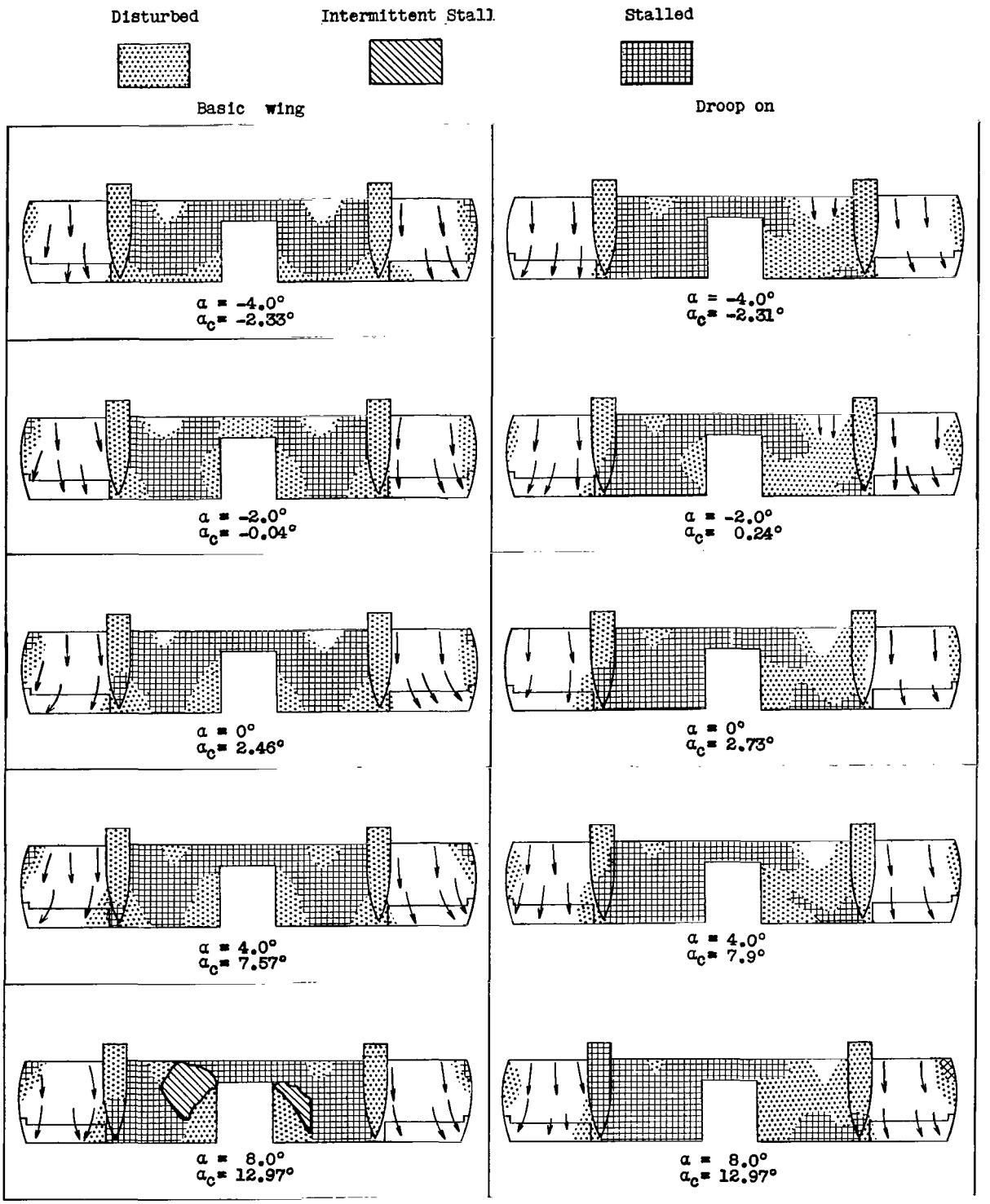

Figure 16.- Stall diagrams for the basic wing and the wing with a modified leading edge (droop on) at $i_w = 50^o$.

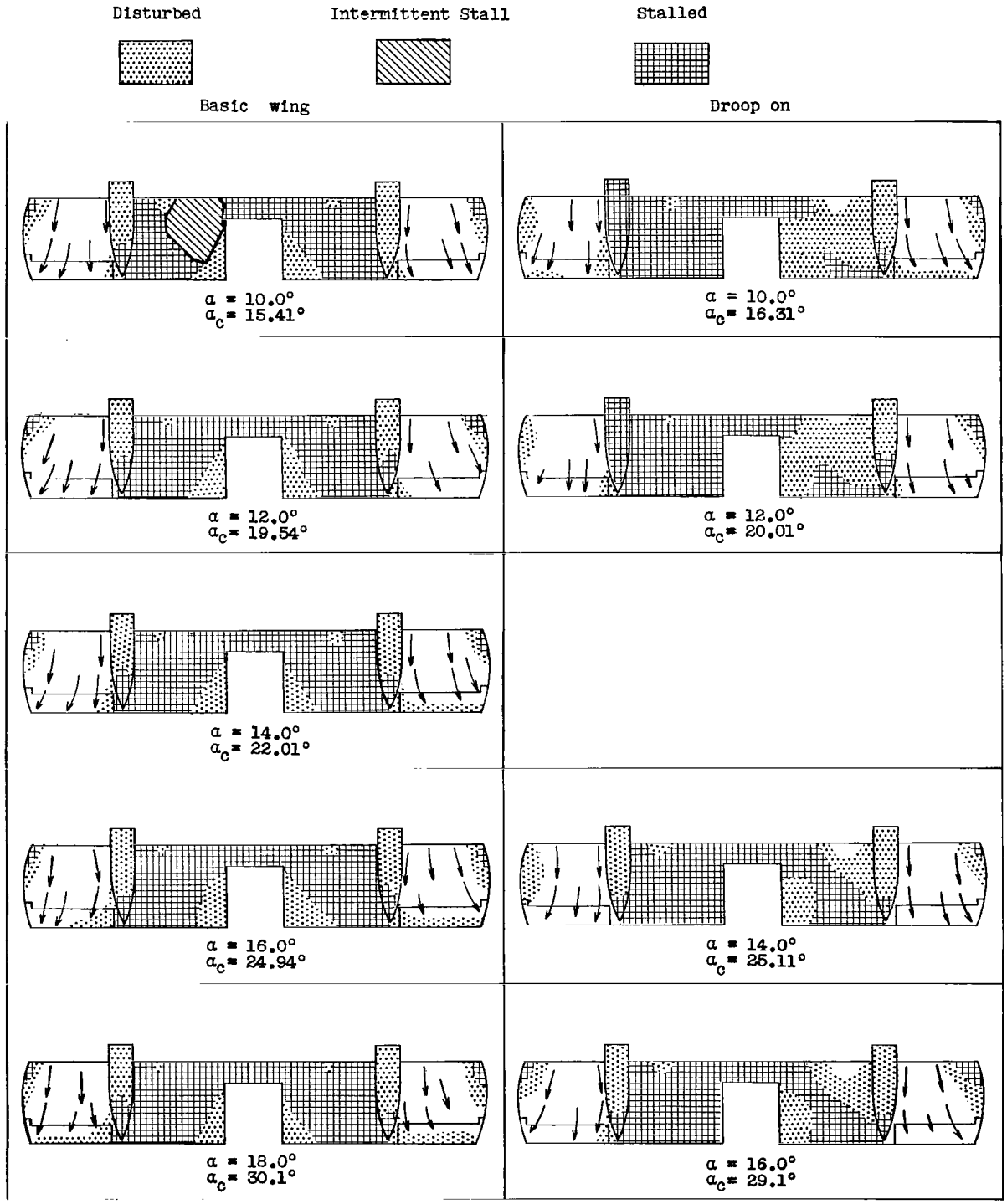

Figure 16.- Concluded.

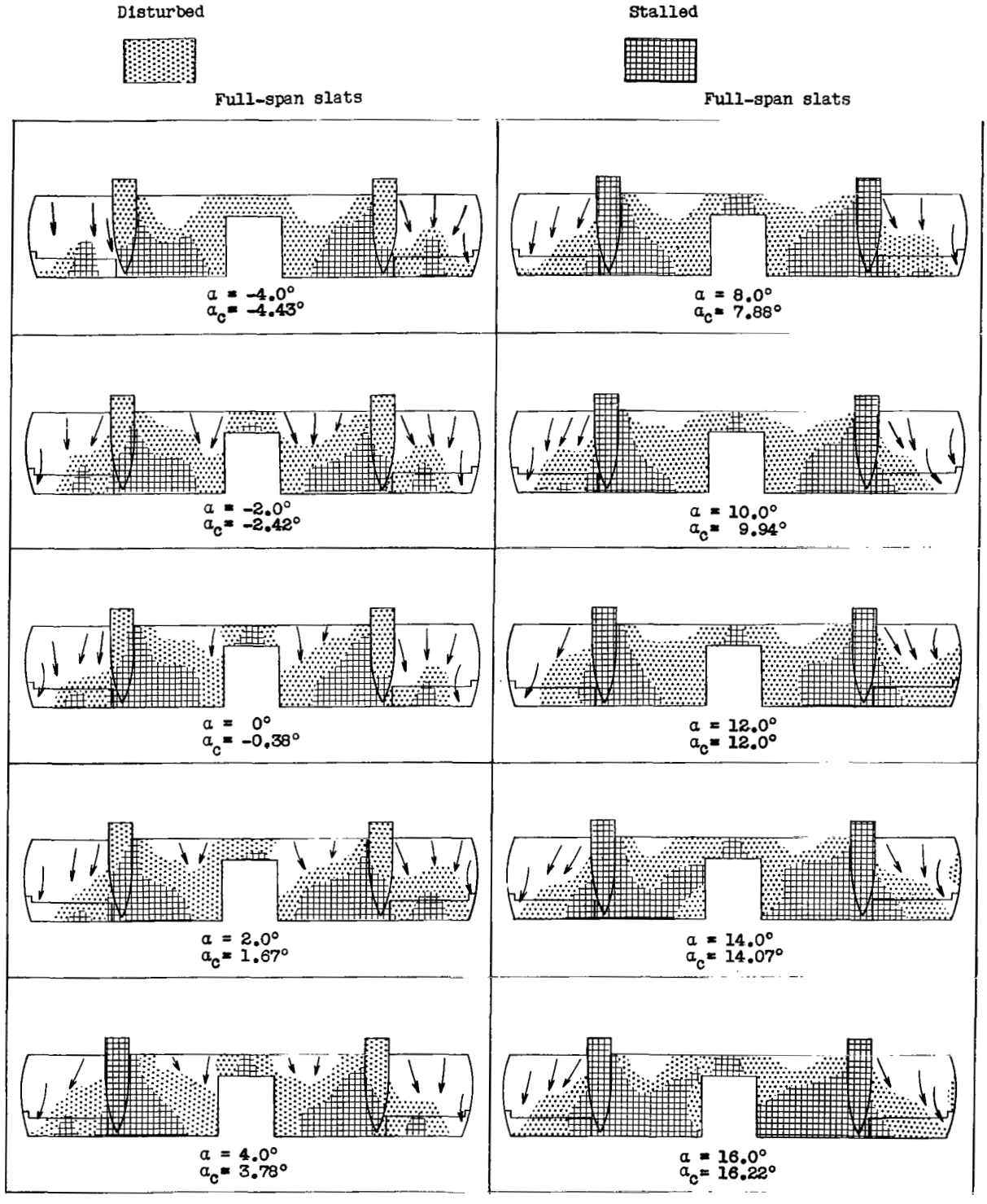

Figure 17.- Stall diagrams for the wing with full-span slats at $i_w = 25°$.

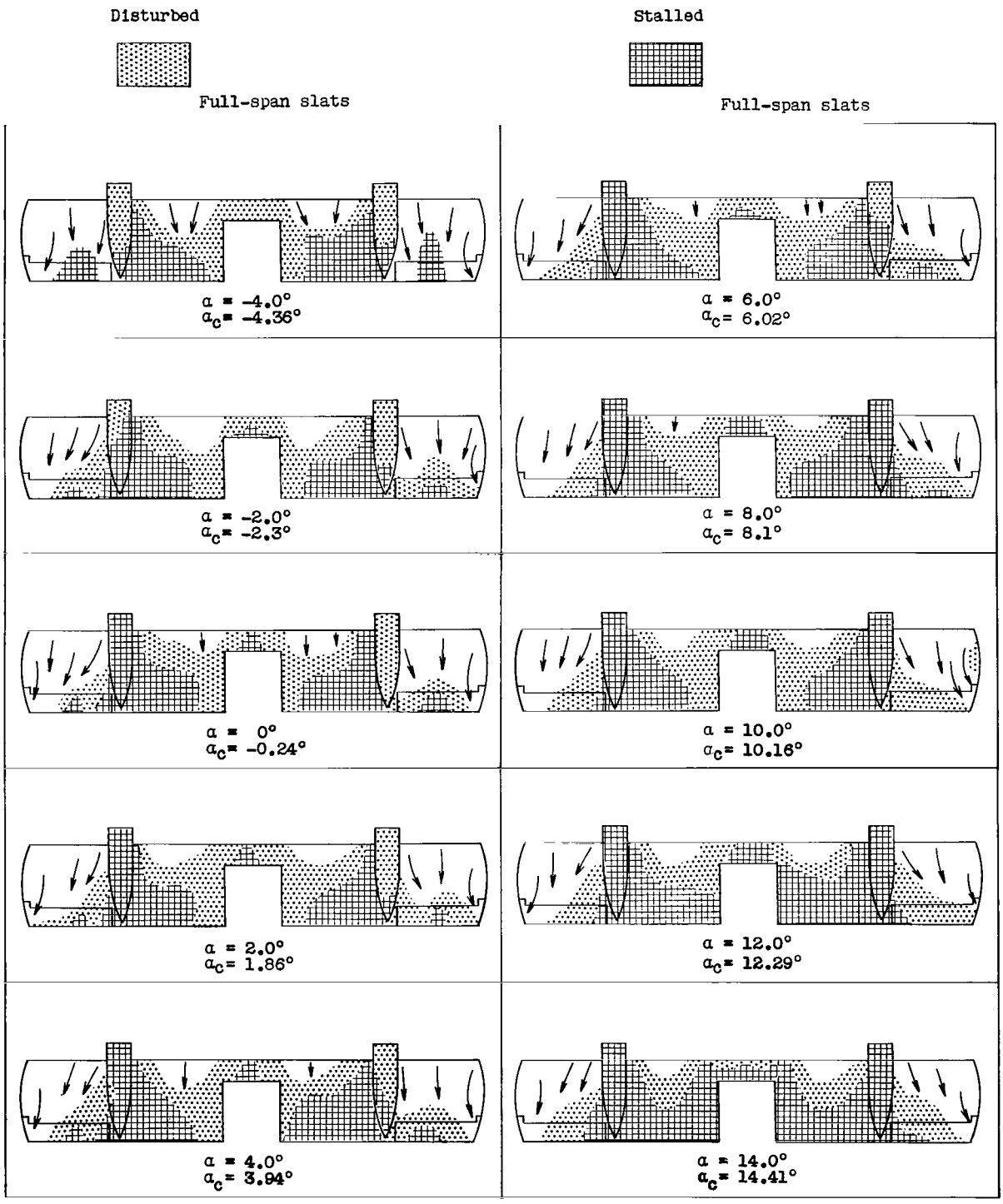

Figure 18.- Stall diagrams for the wing with full-span slats at $i_w = 30°$.

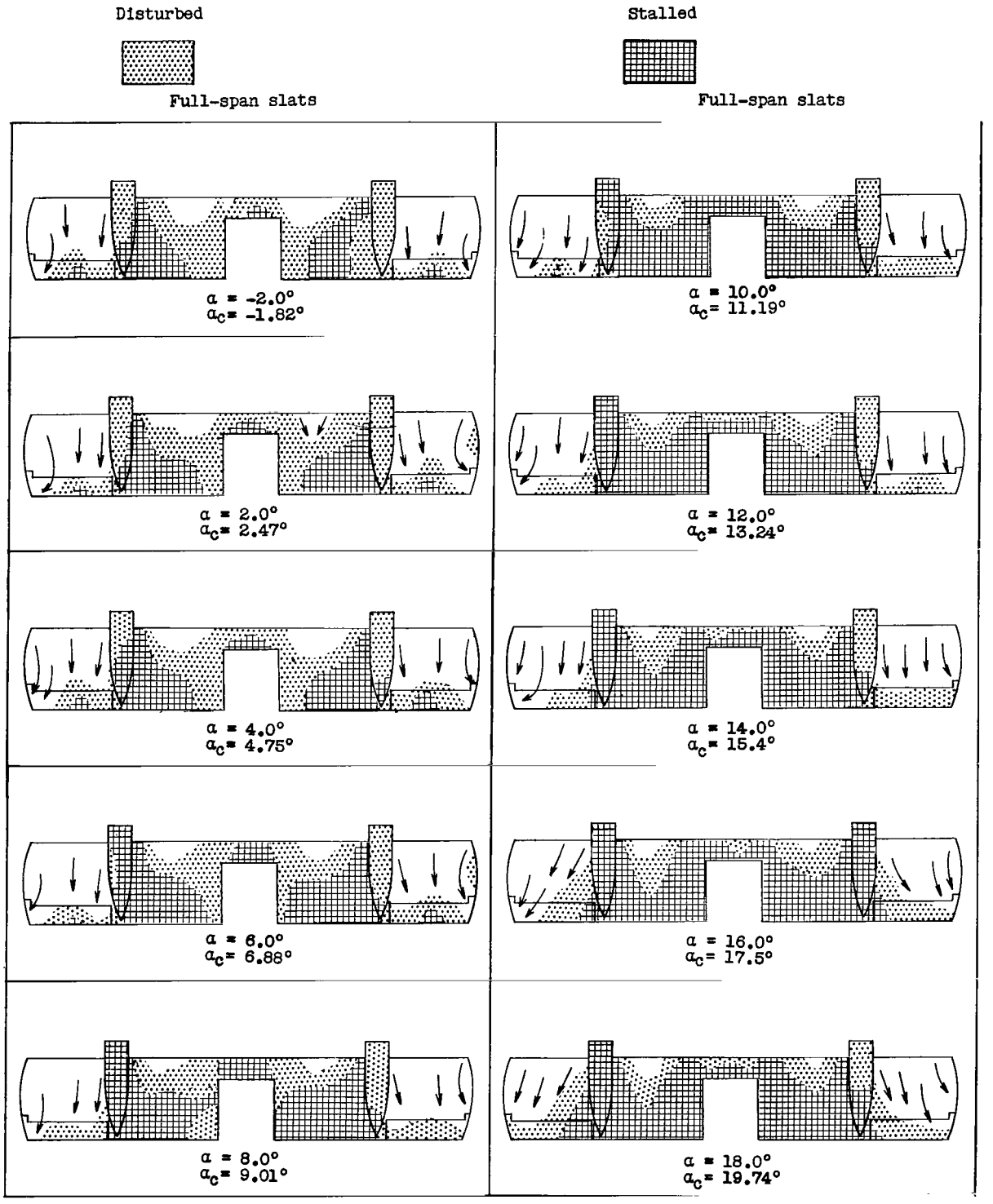

Figure 19.- Stall diagrams for the wing with full-span slats at $i_w = 35^\circ$.

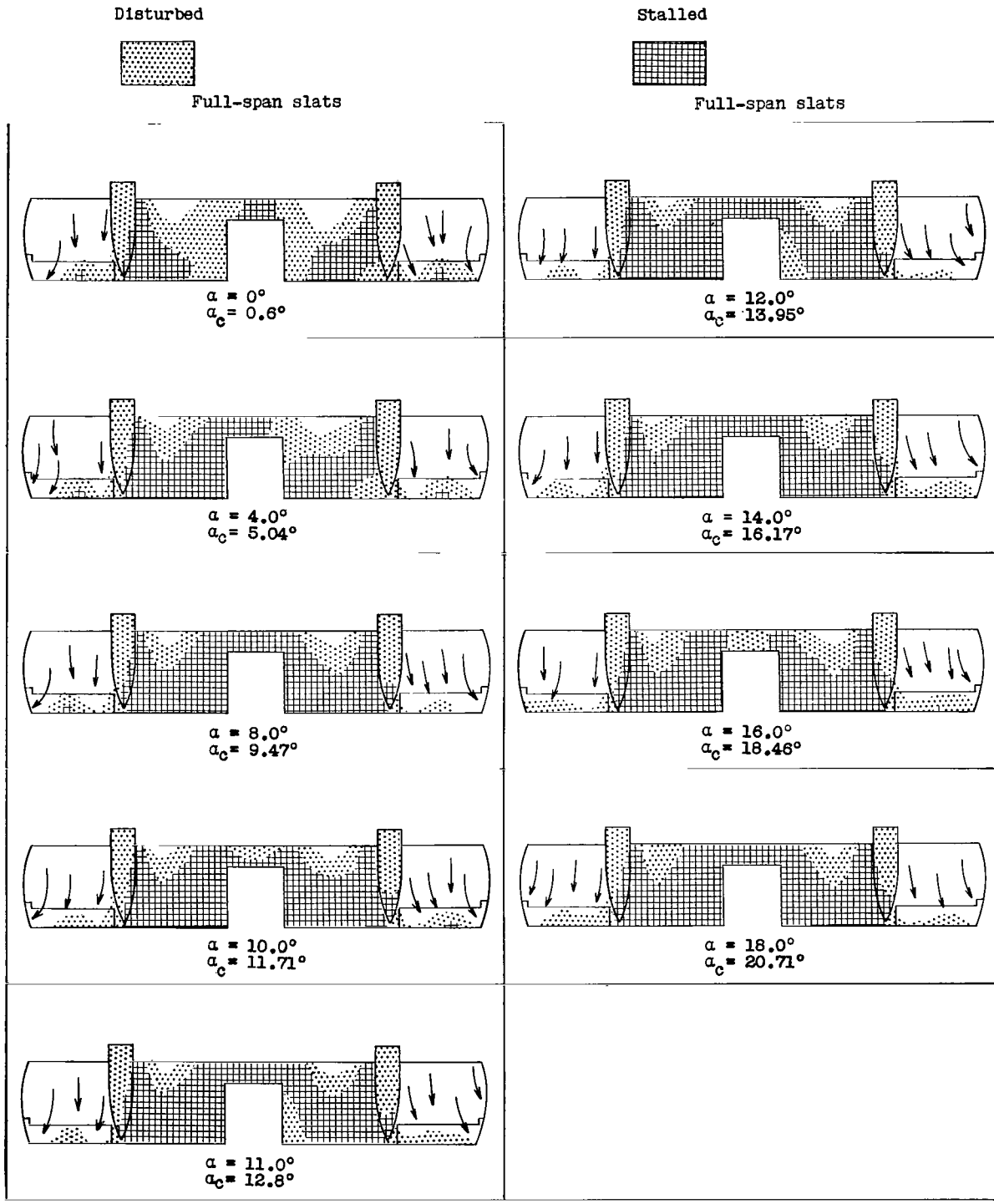

Figure 20.- Stall diagrams for the wing with full-span slats at $i_w = 40°$.

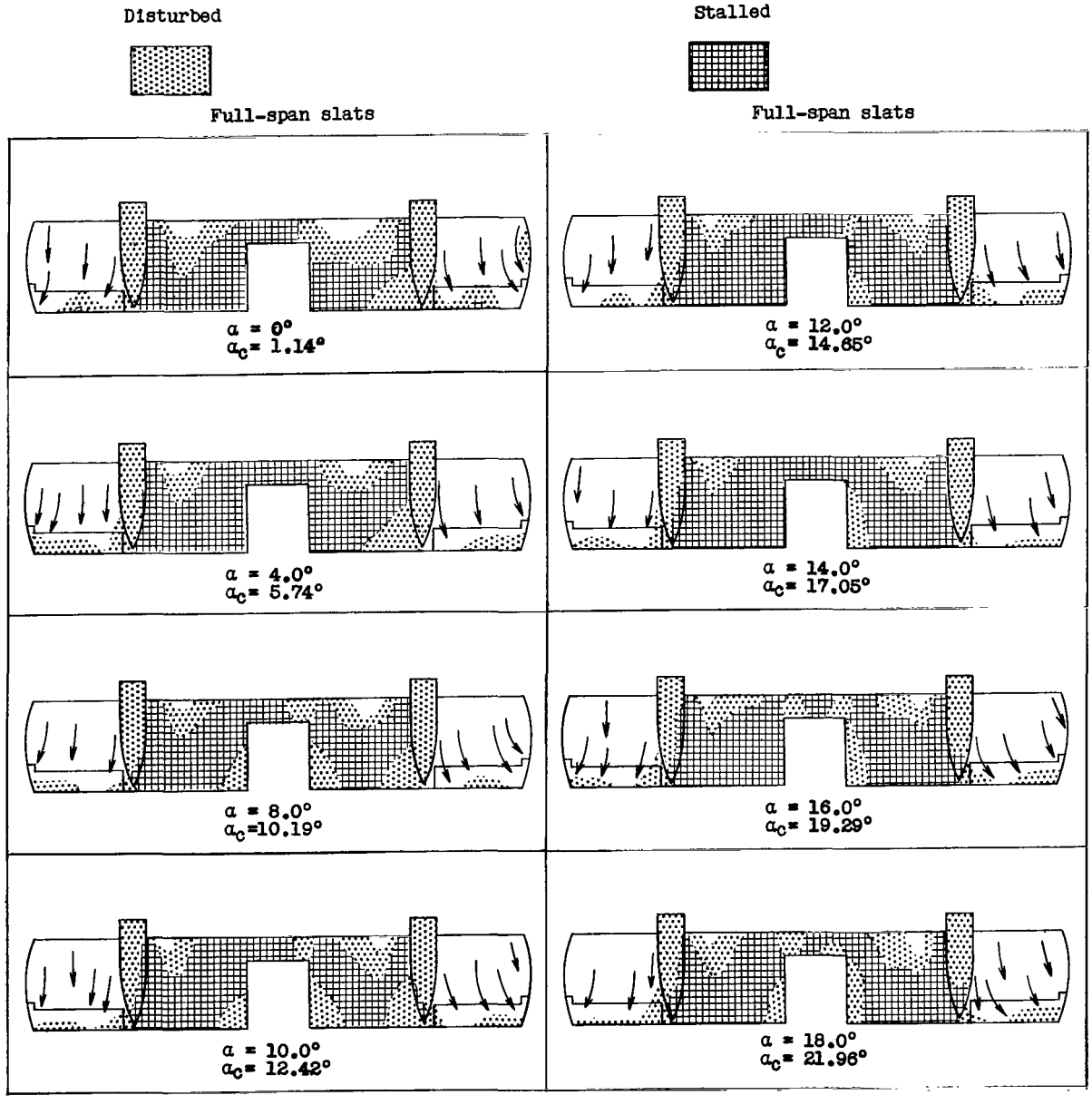

Figure 21.- Stall diagrams for the wing with full-span slats at $i_w = 45°$.

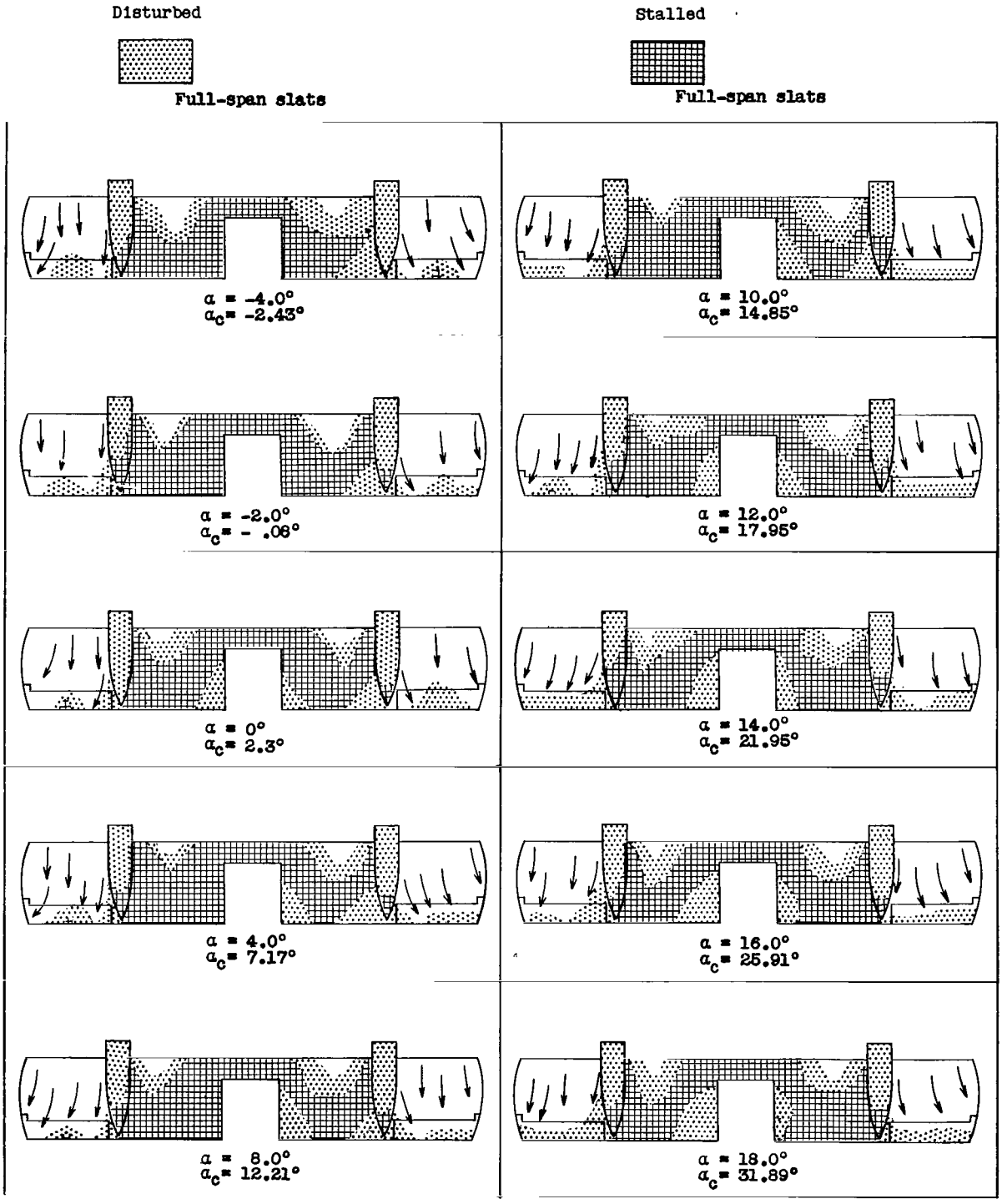

Figure 22.- Stall diagrams for the wing with full-span slats at $i_w = 50°$.

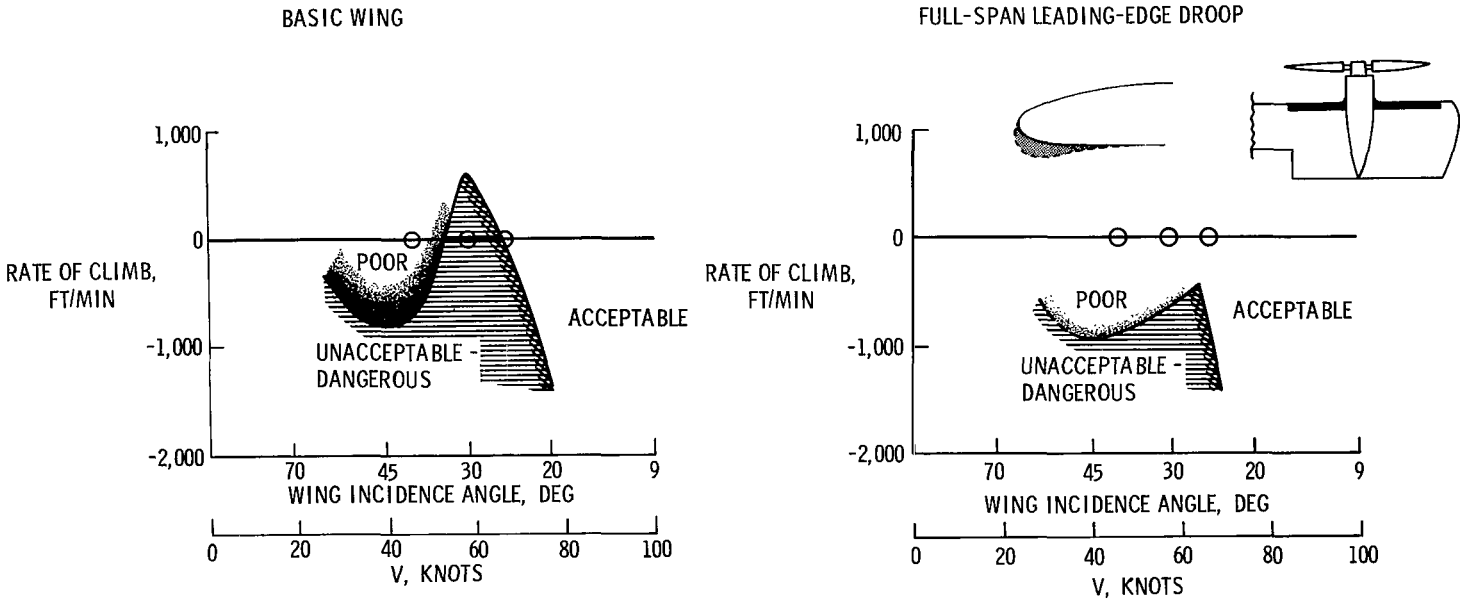

Figure 23.- Flight rate of climb or descent limitations for use in correlation. Weight of airplane, 3,500 pounds.